

Department of Physics and Astronomy

University of Heidelberg

Master thesis in Physics

submitted by

Sophia Milanov

born in Düsseldorf (Germany)

2019

Accreted Globular Clusters in External Galaxies:

Why Adaptive Dynamics won't work

This Master thesis has been carried out by Sophia Milanov at the
European Southern Observatory
under the supervision of
Dr. Glenn van de Ven and Dr. Wilma Trick

Abstract

Many astrophysical and galaxy-scale cosmological problems require a well-determined gravitational potential. Globular clusters (GCs) surrounding galaxies can be used as dynamical tracers of the luminous and dark matter distribution at large (kpc) scales. This M.Sc. project investigates - by means of the Auriga galaxy simulations and in anticipation of high-resolution IFU data of external galaxies - whether a novel action-based approach could provide a constraint for an axisymmetric approximation of the gravitational potential.

In an axisymmetric potential, actions (radial J_R , vertical J_z and angular momentum L_z) are integrals of motion and can be used to characterize and label orbits. In the Milky Way (MW), the assumption that stars in cold streams are on similar orbits was found to be a useful first-order constraint of its gravitational potential. In external galaxies, no individual stars but only GCs can be resolved. One could expect GCs from the same dwarf galaxy (DG) merger event to move at the present time on similar orbits in the host galaxy, analogously to stellar streams in the MW, and should therefore have similar actions in the true (axisymmetric) potential.

We investigate this idea in one galaxy of the cosmological N-body simulation suite Auriga (Grand *et al.*, 2017). As a first step, we present an effective strategy to fit analytic, axisymmetric, time-dependent potential models with slowly varying parameters to the simulation that are good enough to estimate actions.

Then, we select stellar particles born in dwarf galaxies as proxies for GCs and follow the evolution of their orbital actions during the process of merging with a more massive galaxy. These actions show a significant variation over time. As a result, at $z = 0$, the stellar particles accreted in the same merger event show a very extended distribution in action space. We find that minimizing this distribution, however, cannot constrain the true potential since actions and their evolution are affected by complex physical processes during mergers. In local observations, we confirm this result in the stars of Gaia-Enceladus, one of the few DG mergers of our MW that we know of. Their action distribution is smeared out extensively. Based on these results, we propose that modellers need to find and develop more realistic distribution functions for GCs of a single DG merger event in simulations before being able to constrain the gravitational potential of external galaxies using action-based dynamical modelling of GCs.

Zusammenfassung

Viele astrophysikalische und kosmologische Probleme auf Galaxien-Skalen erfordern ein genaues Gravitationspotential. Kugelsternhaufen (GCs), die Galaxien umgeben, können als dynamische Tracer für die Verteilung von Licht und dunkler Materie in großen (kpc) Skalen verwendet werden. Diese Masterarbeit untersucht in der Galaxiensimulation Auriga und in Erwartung hochaufgelöster IFU-Daten externer Galaxien, ob ein neuartiger wirkungsbasierter Ansatz eine Einschränkung für eine axialsymmetrische Approximation des Gravitationspotenzials darstellen könnte.

In einem achsensymmetrischen Potential sind Wirkungen (radiale J_R , vertikale J_z und der Drehimpuls L_z) Bewegungsintegrale und können verwendet werden, um Bahnen zu charakterisieren und zu kennzeichnen. In der Milchstraße (MW) wurde die Annahme, dass Sterne in kalten Strömen auf ähnlichen Bahnen liegen, als nützliche Einschränkung erster Ordnung für ihr Gravitationspotenzial befunden. In externen Galaxien können keine einzelnen Sterne, sondern nur GCs aufgelöst werden. Man könnte erwarten, dass sich GCs aus demselben Zerwgalaxie(DG)-Fusionsereignis auf ähnlichen Bahnen in der Wirtsgalaxie bewegen, analog zu Sternströmen in der MW, und sollten daher ähnliche Wirkungen auf das wahre (axialsymmetrische) Potenzial haben.

Wir untersuchen diese Idee in einer Galaxie der kosmologischen N-Körpersimulationsserie Auriga (Grand *et al.*, 2017). Im ersten Schritt präsentieren wir eine effektive Strategie, um analytische, achsensymmetrische, zeitabhängige Potenzialmodelle mit langsam variierenden Parametern an die Simulation anzupassen, die für die Abschätzung von Wirkungen geeignet sind.

Dann wählen wir Sternpartikel, die in Zerwgalaxien geboren sind, als Stellvertreter für GCs und verfolgen die Entwicklung ihrer Umlaufbewegungen während der Verschmelzung mit einer massereicheren Galaxie. Diese Wirkungen zeigen im Laufe der Zeit einen erheblichen Veränderung. Bei $z = 0$ zeigen die im selben Fusionsereignis angehäuften Sternpartikel daher eine sehr ausgedehnte Verteilung im Wirkungsraum. Wir haben festgestellt, dass das Minimieren dieser Verteilung das wahre Potenzial jedoch nicht einschränken kann, da Wirkungen und deren Entwicklungen von komplexen physikalischen Prozessen während der Verschmelzung beeinflusst werden.

In lokalen Beobachtungen bestätigen wir dieses Ergebnis in den Sternen von Gaia-Enceladus, einer der wenigen Zerwgalaxienfusionen unserer MW, die wir gut kennen. Ihre Wirkungsverteilung ist weitgehend verschmiert. Basierend auf diesen Ergebnissen schlagen wir vor, dass Modellierer in Simulationen realistischere Verteilungsfunktionen für GCs eines einzelnen DG-Fusionsereignisses suchen und entwickeln müssen, bevor sie das Gravitationspotenzial externer Galaxien mithilfe wirkungsbasierter dynamischer Modellierung von GCs einschränken können.

Contents

1	Introduction	1
1.1	The importance of knowing the gravitational potential of galaxies	1
1.1.1	Dark matter	1
1.1.2	Empirical galaxy correlations	4
1.2	Dynamical modelling methods	5
1.3	Some stellar objects in the halos of galaxies	6
1.4	Strategies to model the Milky Way potential	7
1.5	Strategies to measure the mass of external galaxies	8
1.6	Idea of this thesis: Adaptive dynamics of accreted globular clusters .	10
2	An axisymmetric potential for a cosmological galaxy simulation	13
2.1	About the Auriga simulation suite	13
2.1.1	Hydrodynamical Milky Way-like galaxy simulations	13
2.1.2	Auriga	14
2.2	Fitting axisymmetric potential models	16
2.2.1	About the gravitational potential	18
2.2.2	galpy - A python package for galactic dynamics	18
2.2.3	Component decomposition	19
2.2.4	Disk potential	20
2.2.5	Spheroid potential	22
2.2.6	Halo potential	23
2.2.7	Total potential	25
2.2.8	Time evolution	28
2.3	What (not) to do when fitting a gravitational potential to simulations	28
3	Adaptive dynamics: Can actions of accreted globular clusters constrain the gravitational potential?	32
3.1	Integrals of motion	32
3.1.1	Energy and angular momentum	32
3.1.2	Actions	33
3.2	Globular cluster sample selection	34
3.3	Globular clusters in action space	36
3.3.1	Best fit potential	36
3.3.2	Varying potentials	36
3.4	Time evolution of actions	39
3.4.1	Best fit potential	39
3.4.2	Mean best fit potential	39

3.4.3 Energy evolution	44
3.5 Test: evolution of globular clusters on same orbit at $z = 0$	46
4 Discussion	48
4.1 Implications	48
4.2 Actions of observed dwarf galaxy remnants	48
4.3 Context in recent research and literature	50
4.4 Caveats	51
4.5 Future Work	52
5 Summary and conclusion	53
Acronyms	54
References	55
Acknowledgements	64
Statement	65

1 Introduction

Galaxies are complex structures consisting of stars, gas, dust and dark matter (DM) held together by gravity. They have many different shapes, colors and sizes, from low mass dwarf galaxy (DG) to very massive elliptical galaxies, and are in constant change induced by stellar evolution and, with greater impact, by galaxy mergers. We can observe galaxies over a range of scales: from our Galaxy, the Milky Way (MW), over nearby galaxies, where we can still resolve individual parts, to high-redshift galaxies, when the Universe was still very young. This range of galaxies gives insight on galaxy formation and evolution through cosmic times. In their similarities, we can constrain many physical laws about galaxies and the Universe.

1.1 The importance of knowing the gravitational potential of galaxies

One of the most fundamental galaxy properties is its mass. As astronomers, we are interested in the total mass, and also how that mass is distributed, as the mass distribution gives rise to a gravitational potential that governs how the objects in the potential move. Many empirical correlations for galaxies were found which rely on the velocity dispersion, therefore mass, therefore potential of a galaxy.

Galaxies are made up of visible matter (stars, gas, dust) and invisible matter (DM). Through observations of the visible components, we can make educated estimates of their mass, but we cannot measure the mass of DM directly as we cannot see it. However, DM dominates the mass budget of galaxies, so it is very important for our understanding how mass is distributed in galaxies, and throughout the Universe.

1.1.1 Dark matter

DM is invisible in all parts of the electromagnetic spectrum, so it can only be observed indirectly via the gravitational effect it has on objects that we can see. We will now give a very quick overview on the discovery, most promising models, problems and alternatives. This Section closely follows the review chapter on DM in Wilma Trick's PhD thesis (Trick, 2017); the main references are Ostriker and Steinhardt (2003); Maoz (2007) and Mo *et al.* (2010).

History of DM discovery In 1933, Zwicky observed the motions of galaxies in the Coma clusters and found a much higher velocity dispersion than expected from the

1.1. The importance of knowing the gravitational potential of galaxies

visible matter after applying the virial theorem. He introduced the term "dunkle Materie" (German for dark matter) which described the invisible matter. Almost 40 years later, Rubin *et al.* (1970; 1978; 1980) measured rotation curves of first the Andromeda galaxy, our closest spiral galaxy, then of many other edge-on disk galaxies. The visible mass content would lead to rotation curves that decreased towards higher radii r but the rotation curves stayed constant over a large radial range following

$$v_{\text{circ}}(r) = \sqrt{\frac{GM(r)}{r}} \sim \text{constant} \quad (1)$$

with the circular velocity $v_{\text{circ}}(r)$, the gravitational constant G and the total mass within the radius $M(r)$, indicating that there are halos around galaxies built up from invisible matter. Other observational methods also rely on DM, such as strong (e.g. Trick *et al.*, 2016b) and weak gravitational lensing (Tyson *et al.*, 1990; Kaiser and Squires, 1993). DM seems to only interact via gravitational forces but not with electromagnetic radiation and therefore cannot be observed by light. Unfortunately, up to now, there has not been a direct detection of DM in any way which causes great challenges but also brings many opportunities of research.

Cosmological aspects of DM In the current standard model of cosmology, the Lambda cold dark matter (Λ CDM)-model, the Universe is made up of dark energy (Λ) and matter. Recent measurements of the cosmic microwave background by the Planck Collaboration *et al.* (2018) found that dark energy makes up the biggest fraction of the energy density ($\Omega_\Lambda = 0.685$) and matter the rest ($\Omega_m = 0.315$), split up to $\Omega_b = 0.05$ baryonic matter and $\Omega_c = 0.265$ cold dark matter assuming a Hubble constant of $H_0 = 67.27 \text{ km s}^{-1} \text{ Mpc}^{-1}$. Therefore, DM makes up around 84 % of the total matter in the Universe.

Established DM model - cold dark matter Cold dark matter (CDM) was first introduced by Davis *et al.* (1985) through N -body simulations. CDM particles are long-lived and very massive (10 GeV to a few TeV). These particles decoupled very early in the beginning stages of the Universe, already before reionization, and therefore are nonrelativistic. The particles were scattered almost homogeneously throughout the Universe, but with some very small fluctuations. In slightly overdense regions there was a slightly stronger gravitational pull, and in underdense regions slightly less, so particles moved towards the overdense regions and away from the underdense regions. Over time, the particles clustered, forming increasingly larger structures: this bottom-up picture of structure formation is known as hierarchical growth. Baryonic matter moves towards the overdense regions as well and galaxies form in the deepest DM potential wells and along the DM filaments

(Figure 2 shows this structure in the simulation we introduce in Section 2). Relativistic particles would destroy small scale substructure which would lead to larger voids than we observe. Possible particle candidates are Weakly Interacting Massive Particles which are massive particles interacting only via gravity and the weak force. The large scale structure predicted by CDM simulations agrees extraordinary well with the observed clustering of galaxies (e.g. in the Millenium simulations, Springel *et al.*, 2005).

Problems in the current model Although successful in explaining many large-scale phenomena, CDM has some problems on especially smaller scales ($< 1 \text{ Mpc}$) when comparing the predictions of cosmological dark matter only (DMO) simulations to observations (e.g., see the review by Bullock and Boylan-Kolchin, 2017). Some of these problems have been remedied in the recent years.

- **The missing satellites problem:** These simulations predict many more satellites of galaxies in the low-mass end than we observe (Klypin *et al.*, 1999; Moore *et al.*, 1999). This can be explained by the fact that low mass DM halos are extremely ineffective in forming galaxies and go completely dark below a certain threshold mass. In recent simulations analyzed by Sawala *et al.* (2016) including baryons and physical prescriptions, the number of satellites matched the observations.
- **The cusp-core problem:** In these DMO simulations, the halo density profile has a cusp in the center (e.g. Dubinski and Carlberg, 1991; Navarro *et al.*, 1996) while observations find flatter density profiles and cored centers (Flores and Primack, 1994; Moore, 1994). Simulations that include baryons have shown that baryonic feedback processes can flatten cusps into cores (e.g. Pontzen and Governato, 2012).
- **The too-big-to-fail problem** (Boylan-Kolchin *et al.*, 2011): In the DMO simulations, a large population of DM satellites are found with greater central masses than any of the MW's dwarf spheroidals. These subhalos seem to have failed to form galaxies while halos with lower mass were successful. It was first found for the MW but the same problem occurs for Andromeda (Tollerud *et al.*, 2014), other Local Group galaxies (Kirby *et al.*, 2014) and in more isolated lower mass galaxies (Ferrero *et al.*, 2012; Papastergis *et al.*, 2015; Papastergis and Shankar, 2016).

CDM alternatives Many alternatives for CDM have been suggested and many of them have already been ruled out. Some of the alternatives which still are considered are

- **Warm dark matter** These particles should have masses of around 1 keV. The mass grows hierarchically down to a characteristic mass scale, below which the free streaming of the particles prevents halos from forming and the DM is distributed in a smooth background field instead (Smith and Markovic, 2011; Schneider *et al.*, 2013). This theory predicts fewer low-mass DM halos whose densities would be less cuspy in the centers due to higher thermal motions (Bode *et al.*, 2001).
- **Modified Newtonian Dynamics (MoND)**: Milgrom (1983) suggested the idea of a modified theory of Newtonian law of gravity which only has an effect in low accelerations. This theory explains flat rotation curves. A big advantage would be the non necessity of a new mysterious dark particle. Nevertheless, there are examples such as the Bullet cluster (Clowe *et al.*, 2006) which fit perfectly in the CDM universe but struggle to find an explanation in MoND.

1.1.2 Empirical galaxy correlations

In galaxies, many characteristics appear to be correlated. These correlations are usually found empirically by analyzing and combining observational results. Many of the correlations include the mass of a galaxy so once we know the mass we can also make inferences about other properties of the galaxy.

- **Tully and Fisher (1977)** (TF) determined a relationship between the luminosity L of a spiral galaxy and its radial velocity (which is connected to the mass of a galaxy through Equation 1):

$$L \propto (v_{\text{circ,max}})^{\beta} \quad \text{with } \beta = 2.5 - 5 \quad (2)$$

For the radial velocity, they measured the Doppler-broadened 21-cm radio emission line of neutral hydrogen (see Section 1.5).

- **Faber and Jackson (1976)** measured the central radial velocity dispersion σ_0 of elliptical galaxies and found the relation to the luminosity

$$L \propto \sigma_0^4, \quad (3)$$

which is similar to the TF relation of spiral galaxies. The derivation of this relation made simple assumptions such as a uniform mass distribution on the volume of radius R and a constant mass-to-light ratio for all galaxies and equal surface brightnesses. These assumptions are not entirely correct, so there is a large scatter in the data around this relation.

- **The Fundamental Plane** offers a better empirical fit to the data of elliptical galaxies but needs another parameter, the effective radius r_e . It combines radius and luminosity of a galaxy with its gravitational well. Two representations of the fit are (Carroll and Ostlie, 2006):

$$L \propto \sigma_0^{2.65} r_e^{0.65} \quad (4)$$

$$r_e \propto \sigma_0^{1.24} I_e^{-0.82}. \quad (5)$$

Dynamically hot stellar systems, i.e. stellar systems whose stars are on randomized orbits, follow this scaling relation (Misgeld and Hilker, 2011).

1.2 Dynamical modelling methods

As we are not able to observe DM directly, we cannot measure the mass and position of each DM particle. Indeed, our ability to do this for visible matter is limited even in the MW, and impossible in more distant galaxies. Instead, we measure velocities of visible objects that move under the influence of the mass distribution. To connect these velocity measurements to the underlying physics, and hence to infer a gravitational potential, we use dynamical models. Stars in the disk and in the halo of galaxies can be considered as collisionless tracers so the collisionless Boltzmann equation (CBE) (Equation 6) applies to them.

- **Jeans modelling** (Jeans, 1915): The first velocity moment of the CBE relates the velocity ellipsoid of stars at a given position in a galaxy to the gravitational forces and the spatial distribution function (DF) - for an explanation of DFs see Section 2.2.1 - of the stars. One important advantage of this method is that the computation is fast so a lot of different models can be explored. One disadvantage is that the set of Jeans equations is not closed and therefore does not have a unique solution. Therefore, assumptions need to be made and the solution, if found, may give non-physical results e.g. a negative DF (e.g. Eilers *et al.*, 2018).
- **Schwarzschild's orbital superposition approach** (Schwarzschild, 1979): Dynamical models of triaxial galaxies can be made based on observed surface brightness distribution and observed kinematics. Given a potential, an orbit library over the full integral of motion space is constructed. The number/mass/light of stars on a specific orbit are described by a weight. These weighted orbits build up the stellar DF. By comparing the surface brightness and kinematics of the model with the data, the gravitational potential can be recovered. This method is mostly used in external galaxies (Rix *et al.*, 1997;

van den Bosch *et al.*, 2008; Vasiliev, 2013; Zhu *et al.*, 2018).

- **Action-based modelling:** Orbits in axisymmetric potentials can be modelled with DFs which arrange stars in 3D action space instead of 6D phase-space (Binney, 2012b; Bovy and Rix, 2013). The modelling is similar to the Schwarzschild approach. The differences are that it does not numerically integrate orbits but uses orbital actions and tori and instead of orbits weights, the analytic DFs are physically motivated and action-based. Since we need 6D phase-space information to calculate actions it is mainly used in the MW where we can resolve single stars. It is applied to modelling the disk (e.g., Trick *et al.*, 2016a; Trick, 2017) but also to model the stellar halo (see Section 1.4).

1.3 Some stellar objects in the halos of galaxies

Globular clusters (GCs) are self-gravitating, gravitationally bound, gas and DM-free systems of 10^5 to 10^7 stars which are spherically grouped with a typical size of a few parsecs and mass around 10^5 to $10^6 M_{\odot}$. They are therefore much brighter than stars but still very compact so they can be resolved in external galaxies. Since they are some of the oldest stellar populations in the Universe (approximately 13 Gyr old), the chemical composition and kinematics of the GC population contain much information about the assembly history and evolution of the MW and external galaxies. The MW is known to host two distinct GC populations: metal-poor vs. metal-rich / blue vs. red / no net rotation vs. corotation / in halo vs. centrally concentrated / probably accreted vs. in-situ (Renaud *et al.*, 2017 and references therein).

Stellar streams are remnants of tidally disrupted GCs or DGs and are a byproduct of hierarchical galaxy formation. A dynamically cold stream - which means it has a low intrinsic velocity dispersion - usually originates from a GC (Bonaca and Hogg, 2018). Their phase-space distribution is predominantly affected by the galactic gravitational potential and depends less on internal kinematics (Küpper *et al.*, 2010, 2012). They are very thin and more than twice as long as wide so they can be treated as one dimensional in the plane of the sky (Bonaca and Hogg, 2018). Hot stellar streams are created by satellites with higher velocity dispersions such as DGs. The first detected and since then often investigated (hot) stellar stream is the Sagittarius dwarf galaxy and its tidal arms (Ibata *et al.*, 1994).

1.4 Strategies to model the Milky Way potential

There are many different approaches for measuring the mass and the potential of the Galaxy. Due to our position within the MW, some methods which give very good constraints on overall parameters such as e.g. rotation curves of external galaxies (see Section 1.5) cannot be measured as easily. A big advantage is that we can resolve stellar positions and velocities with high precision, especially with *Gaia* (Gaia Collaboration *et al.*, 2016, 2018a,b), which is helpful in both Galactic archaeology and dynamical modelling. These are some of the kinematic and dynamical methods to measure the Galactic mass in the halo (their results are presented in Table 1):

- **Orbits of stellar streams:** Johnston *et al.* (1999) first found that stellar streams contain information about the Galaxy’s gravitational potential. In the case of kinematically cold streams, they move on orbits aligned with the remnant’s orbit (Eyre and Binney, 2011). It is therefore possible to get a direct measurement of the local acceleration close to the stream. So far, dynamical models of four single stellar streams have been used to constrain the mass and shape of the DM halo: the Sagittarius dwarf galaxy (Law and Majewski, 2010; Gibbons *et al.*, 2014; Dierickx and Loeb, 2017), the Orphan stream (Newberg *et al.*, 2010), the GD-1 stream (Koposov *et al.*, 2010; Bowden *et al.*, 2015; Malhan and Ibata, 2018), and the tails of the Palomar 5 globular cluster (Küpper *et al.*, 2015). Since these streams measure local properties, better constraints on the global potential can be achieved by looking at a population of streams (Bonaca and Hogg, 2018).
- **Stellar streams in action space:** The phase-space distribution of tidal streams have the simplest form in action-angle-frequency space (Tremaine, 1999; Helmi and White, 1999). A deeper introduction to actions is given in Section 3. Due to formerly-high computing costs for calculating actions numerically, this approach has been carried out on larger scales only recently after developing new, cheaper methods for action calculations (a review is given in Sanders and Binney, 2016). Sanders (2014) uses a Stäckel-fitting algorithm (Sanders, 2012) to generate probabilistic models of streams to constrain the Galactic potential. Bovy (2014) introduces a new, general method of action-angle-frequency calculation for streams using an orbit-integration-based approximation. In Bovy *et al.* (2016), this method is then for the first time applied individually and combined to the Palomar 5 and GD-1 streams.
- **Tracer dynamics:** Another tracer of the mass of the inner MW halo ($r \leq$

21 kpc) is the GC distribution. There have been a lot of previous studies on this method (for a review see Bland-Hawthorn and Gerhard, 2016) but the best constraints come from recent advances that give us full 6D phase-space information. As part of the second *Gaia* data release, Gaia Collaboration *et al.* (2018b) calculated proper motions (PMs) for 75 GCs; Vasiliev (2018) and Baumgardt *et al.* (2019) later expanded the sample, calculating PMs for 150 and 154 GCs respectively. Watkins *et al.* (2018) use the kinematics of a subsample of GCs in this inner halo to constrain the Galaxy’s mass using a simple tracer mass estimator. Posti and Helmi (2019) employ another approach based on Binney and Wong (2017) by fitting an action-based DF to the 6D phase-space data of 75 GCs to constrain the mass and shape of the DM halo. A very similar approach is carried out in Vasiliev (2018) which mainly differs in assumptions on the assumed form of the halo. PMs are measured by other telescopes as well. Sohn *et al.* (2018) use Hubble Space Telescope PMs to derive the mass of the MW with the same method as Watkins *et al.* (2018) but fewer GCs. Eadie and Jurić (2018) apply a hierarchical Bayesian model to the samples from Vasiliev (2018) and Sohn *et al.* (2018).

To constrain the mass of the outer halo we can use satellite galaxies as tracers. The methods are similar to the ones used for GC estimates. From position and velocity of the most distant dwarf Leo I ($r = 257.8^{+16.8}_{-35.1}$ kpc), Gaia Collaboration *et al.* (2018b) provided a lower limit on the MW mass. Callingham *et al.* (2018) calculate in the hydrodynamical simulations DFs of specific energy and angular momentum, with given 6D phase-space information, which vary according to the galaxy host mass, estimate this mass by a maximum likelihood and apply this method to the MW.

An overview of the results is shown in Table 1. We see, that different methods allow us to constrain the potential at different distances, to the outermost tracers. However, this makes it more complicated to compare the results as masses need to be extrapolated to estimate the total mass. The estimates where q is given use a logarithmic halo potential for the DM halo given by $\Phi(R, z) = v_{\text{circ}}^2/2 \ln(R^2 + z^2/q^2 + \text{core}^2)$ where the core is the radius at which the logarithm is cut and q is the z -flattening parameter which defines the ellipticity (oblate or prolate) of the DM halo (see e.g. Malhan and Ibata, 2018).

1.5 Strategies to measure the mass of external galaxies

In external galaxies, we cannot resolve single stars; in some cases, depending on mass, luminosity and distance of the galaxy, we can resolve objects in the halo such

Table 1: Mass estimation results of the MW for some of the mentioned references. Empty values were not indicated in the papers.

Method	M_{MW} [$10^{11} M_{\odot}$]	at R [kpc]	v_{circ} [km s $^{-1}$] at R_{\odot}	q	Reference
Stellar streams	4.1 ± 0.4	100			Gibbons+ '14
	< 10				Dierickx+ '17
	2.6	60			Newberg+ '10
			224_{-14}^{+12}	$0.87_{-0.04}^{+0.07}$	Koposov+ '10
			$227.3_{-18.2}^{+15.6}$	$0.9_{-0.1}^{+0.04}$	Bowden+ '15
	$1.75_{-0.05}^{+0.06}$	14.5	244.4_{-2}^{+6}	$0.86_{-0.07}^{+0.04}$	Malhan+ '18
	2.1 ± 0.4	19	253 ± 16	$0.95_{-0.12}^{+0.16}$	Küpper+ 15
	1.1 ± 0.1	20		0.94 ± 0.05	Bovy+ '16
Tracer dynamics	$2.2_{-0.03}^{+0.04}$	21.1			Watkins+ '18
	$1.91_{-0.17}^{+0.18}$	20			Posti+ '19
	$6_{-0.09}^{+0.14}$	50			Vasiliev+ '18
	$6.1_{-0.12}^{+0.18}$	39.5			Sohn+ '18
	$3.3_{-0.7}^{+1.1}$	39.5			Eadie+ '18
	$9.1_{-2.6}^{+6.2}$	$257.8_{-35.1}^{+16.8}$			Gaia+ '18b
	$10.4_{-0.14}^{+0.23}$	R_{200}			Callingham+ '18
		not specified			

as GCs, in other cases, we can only observe a galaxy as point source on the sky. To get a constraint on their mass it is useful to measure the rotational velocity of the galaxy (see Equation 1). Different techniques evolved over time and telescope resolution, from measuring one value of the velocity to having spectra for each observed pixel. Some of them are:

- **1D: 21cm line** Hydrogen is the simplest yet most abundant atom in space. The 21 cm line of neutral hydrogen (HI line) is visible through photons which are emitted when relative spins change from parallel to antiparallel. HI is detectable in radio bands in most spirals and some ellipticals. Line-of-sight velocities can be measured from the Doppler shift of these emission lines which give us a constraint on the galaxy's disk maximum rotation velocity and therefore a measurement of the enclosed mass.
- **2D: slit along the major axis** With the slit of a spectrograph aligned along the major axis of a galaxy, it is possible to take stellar spectra at different galactocentric radii. These spectra give us for a population of stars the line-of-sight velocity and the velocity dispersion which both are useful in dynamical modelling. Stars moving towards the observer are blue-shifted, stars moving away are redshifted. From the Doppler shift one can derive the rotational velocity and therefore the mass.
- **3D: Integral Field Unit** Integral Field Unit (IFU) spectrographs observe the 2D field of view and take a spectrum for each pixel at the same time. With that method we gain a 2D velocity map and can learn more about the mass distribution of the observed galaxy. From the spectra of GCs we can extract information with spectral synthesis on age, mass, metallicity and other important characteristics.

1.6 Idea of this thesis: Adaptive dynamics of accreted globular clusters

Context As we have seen, there are several methods of measuring the mass of external galaxies which rely mainly on the rotational velocities measured for unresolved stellar populations. We can try to adapt some of the methods which we use in the MW based on resolved dynamical tracers to external galaxies. These would be strategies which rely on bright, compact objects in the (outer) halos of galaxies, which still can be resolved, GCs.

High resolution IFU data (e.g. from the Multi Unit Spectroscopic Explorer (MUSE, Bacon *et al.*, 2010)) of external galaxies provides us with rich information such as

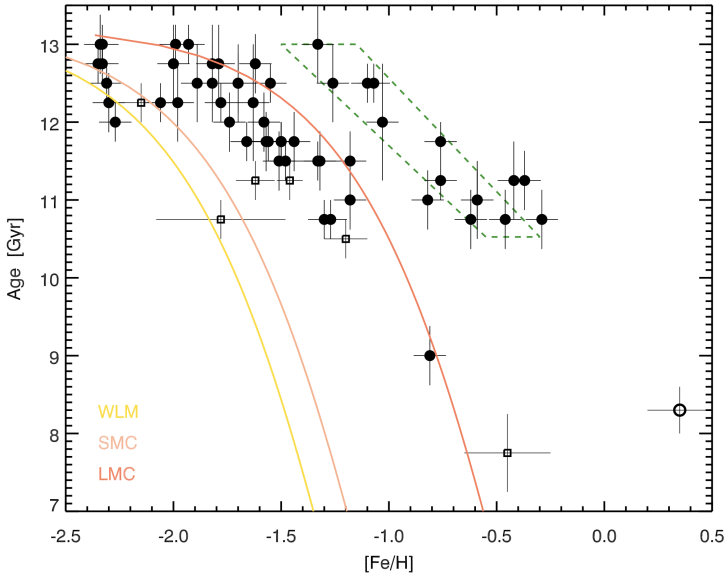


Figure 1: The AMR of MW GCs. The dashed green region predicts the AMR of the MW bulge GCs. The yellow / orange/ red lines are the AMRs of the Wolf–Lundmark–Melotte galaxy and the Small and Large Magellanic Clouds. GCs close to the relations could have formed in DG of such masses and been accreted during the formation of the MW halo. **Credit:** Leaman *et al.* (2013)

high resolution 2D positions, radial velocities of GCs (e.g. in the Fornax galaxies - see Figure 15 of Sarzi *et al.*, 2018) chemical abundances and age from spectral synthesis analysis. Except in the very crowded inner regions, probably all GCs can be observed so there are no problems with completeness and selection effects. Nevertheless, there is no 6D phase-space data available yet as distances and PMs of these GCs in external galaxies would require astrometric precisions beyond what is currently technically possible.

Leaman *et al.* (2013) use the age-metallicity relation of the MW GCs to distinguish them between in-situ and ex-situ formation and to relate them to their progenitor as shown in Figure 1. This method can be used in external galaxies to find GCs accreted from the same satellite.

After the merger, GCs in the MW but also in external galaxies retain a dynamical memory of their progenitor. Their dynamics in the halo depends on the mass and shape of the host. As in Section 1.4, we can use these GCs as tracers to constrain the gravitational potential.

Idea In this work, we test the idea of adaptive dynamics (Binney, 2005) in external galaxies. Adaptive dynamics suggests to use dynamical features (action-angle-frequencies) on similar orbits, be it stellar streams in the halo or resonance moving groups in the disk, and attempts to make these features as sharp as possible in action space. GCs accreted by one DG move on similar orbits. Particles on similar orbits have by definition similar actions. In the wrong potential, the GCs will not move on similar orbits and the spread in actions will be larger. By minimizing their spread we should be able to constrain the gravitational potential of the galaxy. The big assumption that we test in this work is that even though the exact phase-space dis-

tribution of GCs originating from accreted DGs depends on the merger parameters such as the infall direction and velocity, and on the disruption process, they might still live on similar orbits. This implies that the DF of these accreted objects might be close to a δ -function in action space. If this method works, we will gain more insight in the merger history of the galaxies and on the DM and total mass distribution. We test this method in a hydrodynamical cosmological simulation, where we have full 6D phase-space information. To make our investigations comparable to the methods observers use in external galaxies, we fit an analytic axisymmetric potential to the simulation.

Structure This thesis is divided into two major blocks. As a first step we explain in Section 2 how we fit an analytic axisymmetric potential to a hydrodynamical cosmological simulation. At first thought, this seems to be trivial. But it became obvious that there are many issues to consider. The proposed strategies might help future modellers who want to verify their methods, which require a potential, in simulations. Section 3 investigates the main idea of this project: testing if it is possible to constrain the gravitational potential of an external galaxy (where we treat simulated galaxies as external galaxies and apply the same techniques observers use) by minimising the spread in action of accreted GCs. In Section 4 we discuss our results, compare them to current literature, address problems, and give an outlook on how to continue this work. A short summary and conclusion is given in Section 5.

2 An axisymmetric potential for a cosmological galaxy simulation

We first give an overview about hydrodynamical simulations in general and the Auriga simulations in particular in Section 2.1. In Section 2.2, we explain how we fit analytical potentials to Auriga galaxies and we finish in Section 2.3 with an overview of tricky parts in that process.

2.1 About the Auriga simulation suite

2.1.1 Hydrodynamical Milky Way-like galaxy simulations

To understand how our Universe and everything in it has formed and evolved, astronomers use simulations of it two ways: trying to match observations of real galaxies and thus checking if the input "recipes" are correct, and predicting observations which then are to be tested by observers. These simulations stretch over a large range of astronomical scales, from stars and planets to the evolution of the cosmic web, but also over different numerical techniques, from more empirical, statistical Monte-Carlo methods to cosmological hydrodynamical N -body simulations.

Cosmological simulations try to create the "Universe in a box". The implemented hydrodynamics follow gas and star formation and reveal properties and internal structures of galaxies. To learn more about the formation and evolution of galaxies, these hydrodynamical cosmological simulations are a rich tool to exploit. The implementation of these simulations is very complex and requires many assumptions. A calibration of the theoretical results vs. observations is always needed. However, if successful in creating observed properties, they can come into predictive regimes where there is no tuning based on observations. These findings then need validation from the observers. These galaxy simulations are therefore powerful tools for observers and modellers.

Hydrodynamical zoom-in galaxy simulations are carried out by first evolving DMO halos according to the chosen DM scenario and adopted cosmological parameters from a very high redshift to redshift 0. Then, to find MW like halos, one takes the most isolated halos in the mass range of the MW halo - $1 < M_{200}/10^{12}M_\odot < 2$ - of the simulated sample. In these halos, particles within a certain range are followed back to their initial conditions. In re-simulations, they are split up into a DM part and gas cells. With an elaborate physics model, these gas cells produce stars within an empirical threshold and therefore galaxies form. DM forms in a web along filaments and stars follow the DM distribution.

2.1. About the Auriga simulation suite

This work uses the Auriga (Grand *et al.*, 2017, hereafter G+17) simulations, which try to recreate spiral galaxies such as our own. In Figure 2, we show the distribution of DM in grey and stars in colors of one selected simulated galaxy (halo 24) in which we carry out all investigations. The most bound particle is chosen to be the center at $(x, y, z) = (0, 0, 0)$. The filaments of the DM distribution are clearly visible. The stellar particles settle along these filaments and clump inside the densest DM structures.

2.1.2 Auriga

Auriga is a magneto-hydrodynamical zoom-in simulation of an isolated MW like galaxy. It is build with the moving-mesh code **AREPO** (Springel, 2010) and includes galaxy physics, active galactic nuclei feedback and magnetic fields. Its goal is to match the observables of the MW today and to produce its history which can be compared to observations of spiral galaxies in earlier stages of development. All 30 galaxies are run in normal resolution (DM particle mass: $m_{\text{DM}} = 3 \cdot 10^5$; baryonic matter particle mass: $m_b = 5 \cdot 10^4$) and 3 selected are run in low ($m_{\text{DM}} = 2 \cdot 10^6$; $m_b = 4 \cdot 10^5$) and high resolution ($m_{\text{DM}} = 4 \cdot 10^4$; $m_b = 6 \cdot 10^3$) as well (G+17). They are consistent over these three resolution levels and therefore do not rely on numerical parameters but only on physical ones. Auriga is one of the first simulations where this is accomplished. The snapshots go from redshift 13.3, which is close to the beginning of the universe, to redshift 0, today. At redshift $z = 0$, different galaxy shapes have evolved. Most of them are spirals but a few are in a merger process. All galaxies have a rich merger history. G+17 find that many properties of the MW and MW like external galaxies are reproduced by these simulations, such as the mass distribution and the circularity distribution. Others are found to be lower than observed, such as the star formation rate–stellar mass relation, however, results are consistent for present-day metallicities, mean stellar ages and colours. The set-up and the results of this set of simulations make Auriga one of the most advanced and comprehensive magneto-hydrodynamical galaxy simulations and a very fruitful sample to carry out our investigations.

In Figure 3, we present the distribution of stellar particles in $x - y$ and $x - z$ direction of the main galaxy in halo 24 and its associated DGs at redshift $z = 0$. Over the course of time, many DGs already merged with the main galaxy. These make up some of the galaxy’s mass and the DG stars involved in these mergers are investigated in Section 3.

A face-on and edge-on view of the main galaxy is presented in Figure 4. We can see

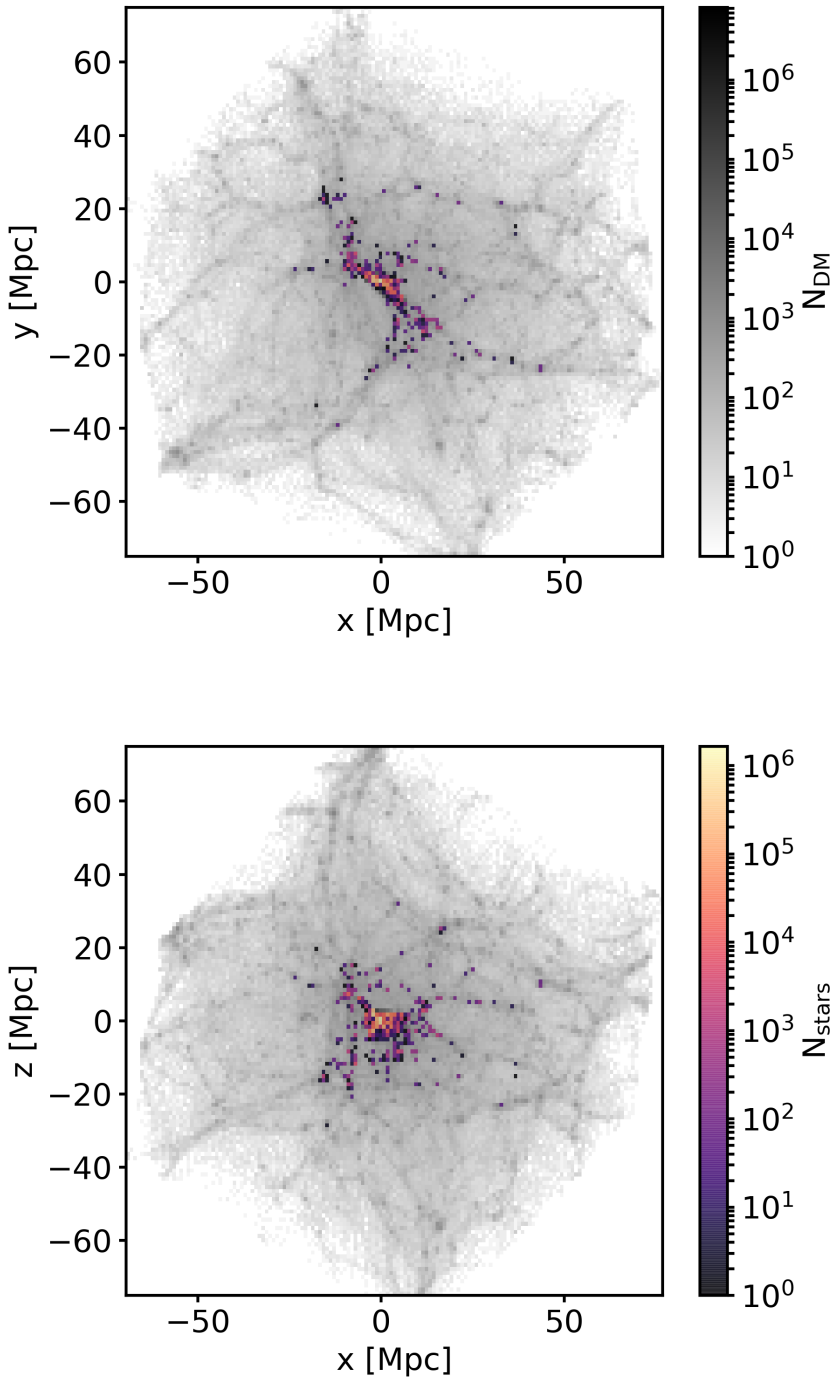


Figure 2: DM (grey) and stellar (colors) particle distribution of the whole simulation Auriga24 at $z = 0$. The DM forms the cosmic web, where the mass gathers along its filaments. Baryonic matter also follows these structures. At the most massive parts of the DM distribution, the most stellar particles fell in. This structure is typical of hydrodynamical galaxy simulations.

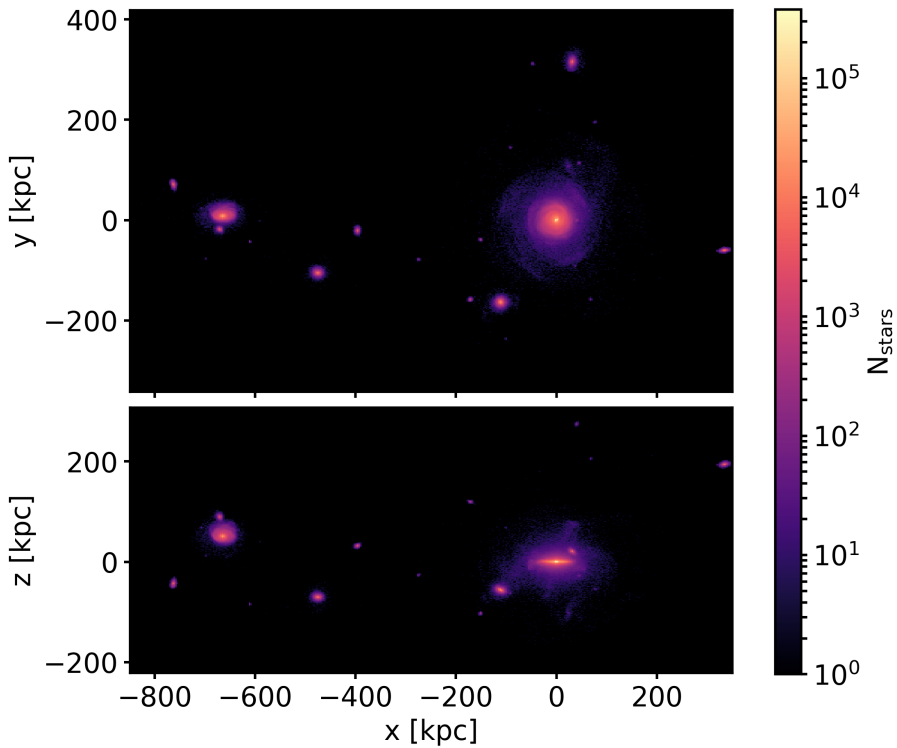


Figure 3: Stellar distribution of 0th halo at $z = 0$. The main galaxy is centered at $(0, 0, 0)$. There are many DGs around the main galaxy which will eventually merge with it. In the evolution of the simulations, this galaxy has built up mass by merging with DGs.

axisymmetric features such as bulge and disk and clear non-axisymmetric features such as a bar and spiral arms. This galaxy resembles the MW and other late-type galaxies.

2.2 Fitting axisymmetric potential models

We would like the best fit potential model of this galaxy to be an analytic, axisymmetric, multi-component potential so that we consider these simulations as observers treat external galaxies, since they mostly fit external galaxies with these models (e.g. Geehan *et al.*, 2006). We need to point out that the galaxy did not evolve in isolation but went through many mergers and therefore its potential is neither analytic nor axisymmetric but has a lot of substructure. The fit is only an approximation. Also the simulation is self-consistent so changes in potential influence the velocities of the objects inside and changes on the positions of the objects will change the gravitational potential. Since we fit a potential to each snapshot we have a time-dependent potential. The routine and results in this Section are for the $z = 0$ snapshot but the same routine was applied for all snapshots since a lookback time of 10.5 Gyr. We also need to include a disk and bulge decomposition which is not

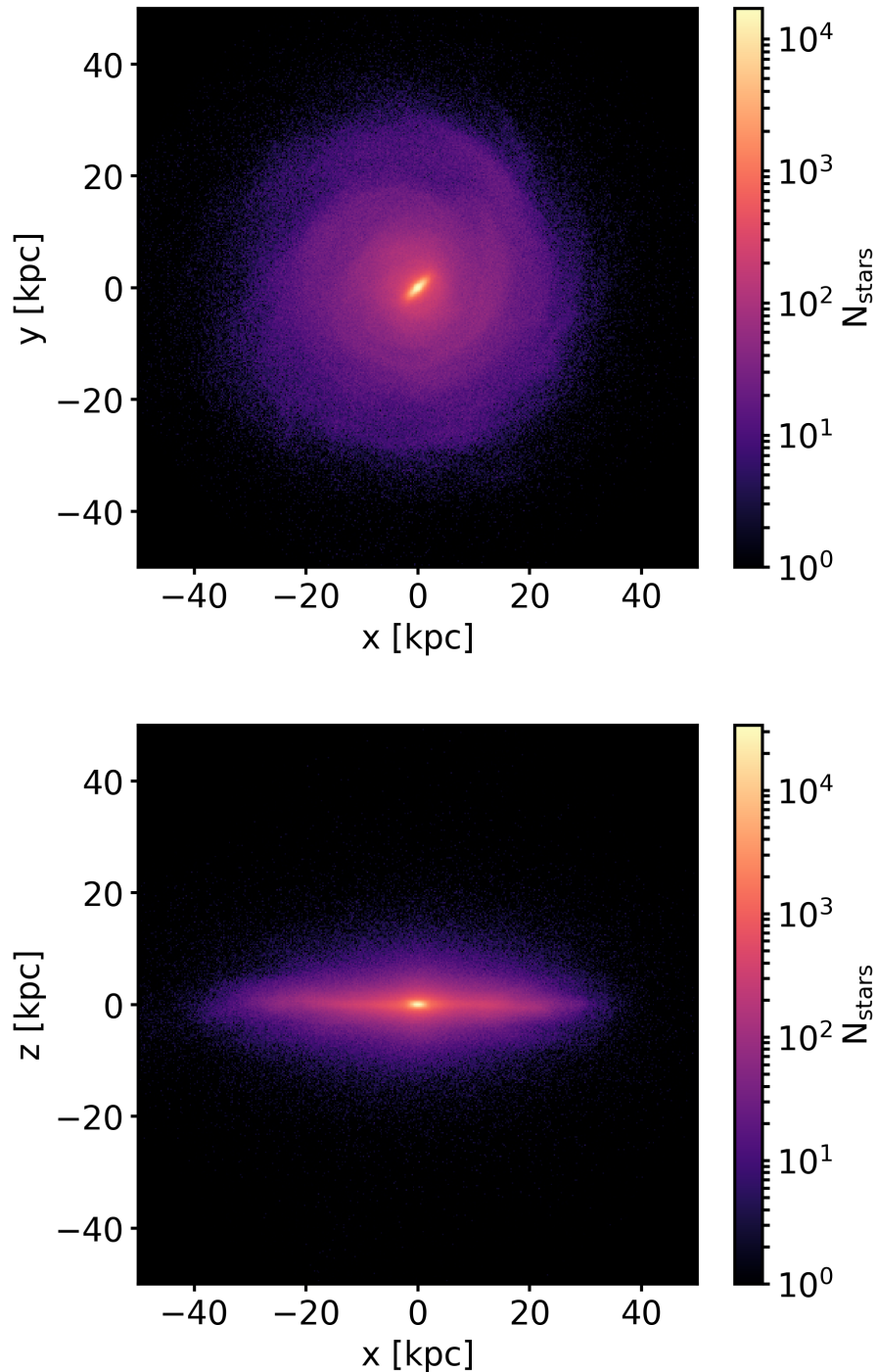


Figure 4: Stellar distribution of main galaxy at $z = 0$. In the upper panel, the galaxy is seen face-on. There, the presence of non-axisymmetric substructure such as spiral arms and a bar is visible. In the lower panel it seen is edge-on. Disk and bulge are clearly present.

natural in a cosmological simulation. As the gas evolves in cells, we cannot calculate its density easily. Therefore, we do not consider it in our potential fits. Since we want to recreate observers way of looking at galaxies we do not need to include gas as observers in e.g. Multi-Gaussian Expansion fits (Monnet *et al.*, 1992; Emsellem *et al.*, 1994), that are used in Jeans modelling (Cappellari, 2008; van de Ven *et al.*, 2010), also only take stellar light into account.

2.2.1 About the gravitational potential

The distribution of stars can be described by their DF, $f(\mathbf{x}, \mathbf{v})$ which describes the observed positions and velocities of the stars. They can act as tracers of the gravitational potential $\Phi(\mathbf{x})$. Stars in the disk and the stellar halo are to an extremely good approximation a "collisionless fluid". For these stars, the CBE describes their motions:

$$\frac{df}{dt} = \frac{\partial f}{\partial t} + \frac{\partial f}{\partial \mathbf{x}} \cdot \frac{d\mathbf{x}}{dt} + \frac{\partial f}{\partial \mathbf{v}} \cdot \frac{d\mathbf{v}}{dt} \quad (6)$$

$$= \frac{\partial f}{\partial t} + \nabla_x f \cdot \mathbf{v} + \nabla_v f \cdot \mathbf{a} = 0. \quad (7)$$

Applying Newton's gravitational law $\mathbf{F} = -m\nabla\Phi(\mathbf{x}) = m\mathbf{a}$ to the last part of the equation and taking the Poisson equation into account to connect $\Phi(\mathbf{x})$ with the total mass we get the important equations:

CBE :	$\frac{df}{dt} = \frac{\partial f}{\partial t} + \nabla_x f \cdot \mathbf{v} - \nabla_v f \cdot \nabla_x \Phi(\mathbf{x})$	(8)
-------	--	-----

Poisson :	$\nabla \cdot \nabla \Phi(\mathbf{x}) = \nabla^2 \Phi(\mathbf{x}) = 4\pi G \rho(\mathbf{x})$	(9)
-----------	--	-----

with the gravitational constant G and the total mass density of stars, gas and DM, $\rho(\mathbf{x})$. If the system is in "steady state", $\partial f / \partial t = 0$, distribution functions that are functions of the integrals of motion (IoMs) solve Equation 8 (see Section 3). The Poisson equation, Equation 9, is used to link densities and potentials in the upcoming descriptions of the potentials of the single components and presents a direct link between the gravitational potential and the total mass.

2.2.2 galpy - A python package for galactic dynamics

galpy (Bovy, 2015) is a well tested and well documented python package for galactic dynamics that is being developed on <http://github.com/jobovy/galpy>. The latest documentation can be found at <http://galpy.readthedocs.org/en/latest/>. It includes analytic spherical, axisymmetric and ellipsoidal triaxial potentials and

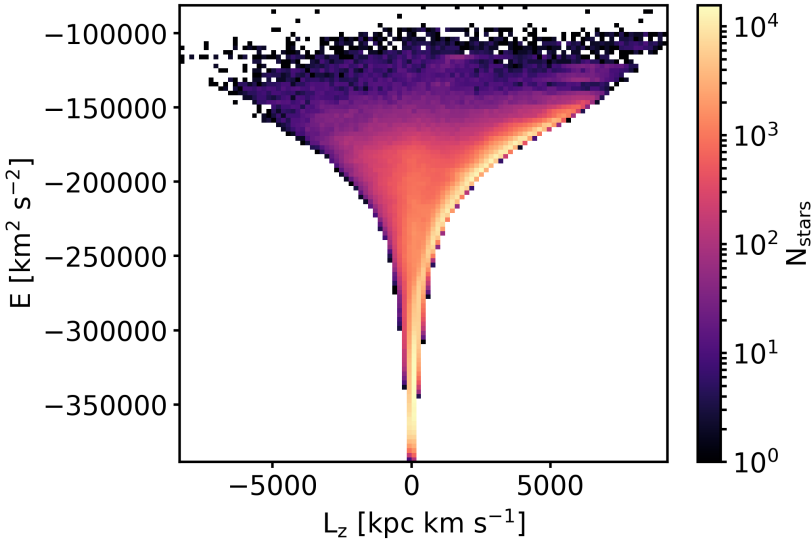


Figure 5: Energy vs angular momentum of all stellar particles within the galaxy radius. $L_{z,\max}$ is the right border of the distribution. Stars which lie close to that edge are therefore disk stars which is very good visible in the overdensity there.

fast routines, additionally implemented in C, for the calculation of orbits, action-angles and DFs. `galpy` has its own internal units which have to be considered and understood before using it.

In this work, we first fit a set of analytic potentials to the simulation which is described in the remainder of this Section. Then, we calculate actions of accreted GCs in a variety of potentials in `galpy` and investigate the results in the next Section.

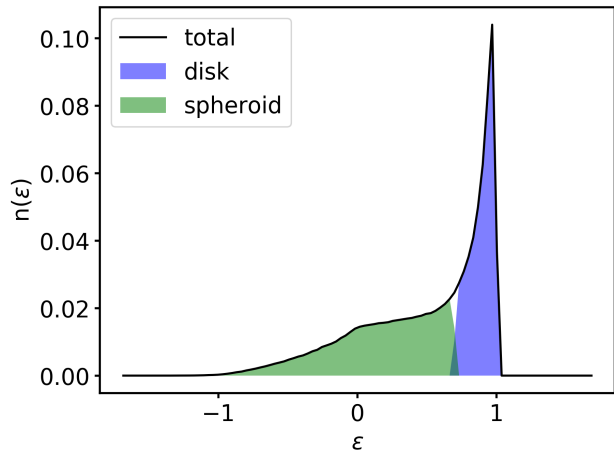
2.2.3 Component decomposition

To fit a potential to each component, we first need to decompose the different parts. We assume that all DM particles belonging to the main galaxy make up its halo. The stellar particles belong to either the central spheroid or the disk. We distinguish these components by the use of the circularity parameter (Abadi *et al.*, 2003)

$$\epsilon = \frac{L_z}{L_{z,\max}(E)} \quad (10)$$

where $L_{z,\max}(E)$ is the maximum angular momentum allowed for the orbital energy E . The distribution of all stars in $E - L_z$ is plotted in Figure 5. The overdensity on the right edge of the distribution is where $\epsilon \approx 1$. Therefore, these are the disk stars. $\epsilon = 1$ is a prograde circular orbit in the disc plane. $\epsilon = -1$ is a retrograde circular orbit in the disc plane. $\epsilon \sim 0$ is an orbit with a very low z -component of the angular momentum which may be highly inclined to the disc spin axis and/or be highly eccentric.

Figure 6: Decomposition of stellar disk and spheroid by their circularity. It was carried out for all stellar particles within the galaxy radius. The black line represents the total circularity. The green area is the the spheroid component and the blue is the disk component. The disk particles were selected by having a circularity above 0.7. The disk to total number ratio is 0.47. The overlap is due to the way how this plot is made, however, in the analysis, there is a strict cut at 0.7.



G+17 use two different methods two distinguish the components and to get their mass ratio:

1. Under the assumption, that the bulge has zero net rotation, mirror negative ϵ as bulge material, the rest belongs to the disk.
2. All particles with $\epsilon >$ constant are assigned to the disk, where constant = 0.7 is set heuristically.

G+17 find that the first method generally overestimates the disk-to-total (D/T) ratio while the second approach underestimates it by choosing only kinematically very cold particles. Since we do not only want to get the mass ratio of D/T but also want to tag each particle clearly, we use the second method. Nevertheless, the true assignment lies somewhere between these methods.

In Figure 6, we show a histogram of the circularity with our decomposition. The blue part is the disk portion while the green part is the spheroid. Together they add up to the black solid line, the total number. The D/T ratio is 0.47.

Since we can assign the particles to be in the spheroid or disk easily, we use this decomposition to find the disk and spheroid, shown in Figure 7, where we fit the stellar components of the potential to.

2.2.4 Disk potential

We fit the disk with a Miyamoto and Nagai (1975) (MN) potential following the profile

$$\Phi(R, z) = -\frac{GM}{\sqrt{R^2 + (a + \sqrt{z^2 + b^2})^2}} \quad (11)$$

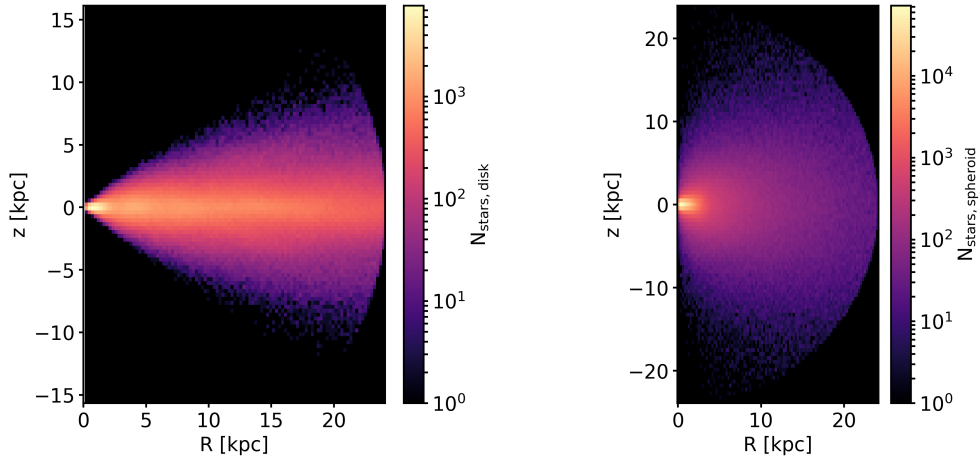


Figure 7: Spatial distribution in radius and height of the decomposed stellar particles. *Left panel:* Disk stars; *right panel:* spheroid stars. The shapes of the distributions are as expected. The disk is clearly visible even though it flares at higher R . The spheroid is centrally concentrated.

with scale length a and scale height b , which provides a disk with a finite thickness. If $b \rightarrow 0$, the disk will be infinite thin and if $b \rightarrow 0$ and $a \rightarrow 0$, the potential has a spherical density distribution. b/a therefore defines the flattening of the system. It is a rather simple model with only small computational costs as forces and densities can be calculated analytically from Equation 11. Therefore it is widely used. It has limitations in the mid-plane ($z = 0$) at high R as the density behaves as R^3 for $R \gg a$ and the large-radius density fall-off is therefore simply a power-law of R rather than exponential.

To fit the disk potential, we bin the stellar disk in (R, z) in step sizes of 0.5 kpc and calculate the density of each bin. Then, we fit the MN density (Equation 11) to the binned data using the `scipy` (Jones *et al.*, 2001) routine `optimize.curve_fit`. For the MN potential, we have the scale length a_{MND} , the scale height b_{MND} and the contribution to the total circular velocity $v_{0,\text{MND}}$ at $R_0 = 8$ kpc as fit parameters. The best fit parameters are listed in Table 2.

The best fit is shown in Figure 8. In the left panel, we see the binned data. Due to the kinematic selection of disk particles, the disk appears to be flaring. This is negligible since the density falls off quickly above an absolute height of 1.5 kpc. At the black parts of the histogram, there was no data. Therefore, the weights of the fit lay on the actual disk. In the middle panel, we show the binned density of the best fit MN profile. We can clearly see the disk. Since it is an analytic potential, the density can be calculated for every bin in (R, z) . In the right panel, the relative errors $\Delta_\rho = (\rho_{\text{fit}} - \rho_{\text{data}})/\rho_{\text{data}}$ are plotted. In the edges of the data, these errors are very high. This is probably due to selection effects and cutting the data there while the fitted density is still smooth there. In the disk and outer regions, the relative

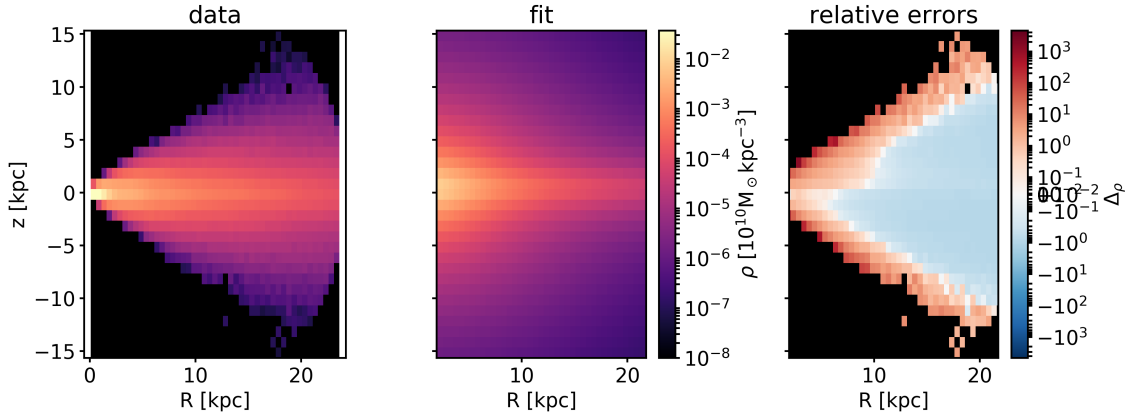


Figure 8: Density fit of the MN profile to the disk. *Left panel:* in (R, z) binned mass density of the simulation data. *Middle panel:* in (R, z) binned mass density of the best fit MN profile. *Right panel:* relative errors $\Delta_\rho = (\rho_{\text{fit}} - \rho_{\text{data}})/\rho_{\text{data}}$ of the best fit. The relative errors are very high at the edges of the data distribution. In the disk and the outer regions, the error is smaller.

error is smaller than at the edges. We discuss problems with the disk fit in Section 2.3. Even though the errors are quite big, we think this is the best fit of the analytic MN potential to the non-analytic and selected-through-decomposition disk.

2.2.5 Spheroid potential

For the central stellar spheroid, we apply a Hernquist (1990) potential which has the density

$$\rho = \frac{M}{2\pi r} \frac{1}{(r + a)^3} \quad (12)$$

where M is the stellar mass of the spheroid and a is its scale length. It has a gentle power-law cusp and at large radii, it declines like r^{-4} . Hernquist (1990) has shown that it reproduces properties of elliptical galaxies and spherical bulges.

Since the Hernquist density is spherically symmetric, we bin the spheroid particles in logarithmic bins in the spherical radius r and in the density ρ . We fit Equation 12 to the binned data using `optimize.curve_fit` again. The data and best fit densities are shown in Figure 9. While in the inner part the fit does not match the data too well, in the outer parts it does. Since most of the particles we investigate in Section 3 are more far away from the center than 10 kpc, the fit is acceptable to carry out this analysis.

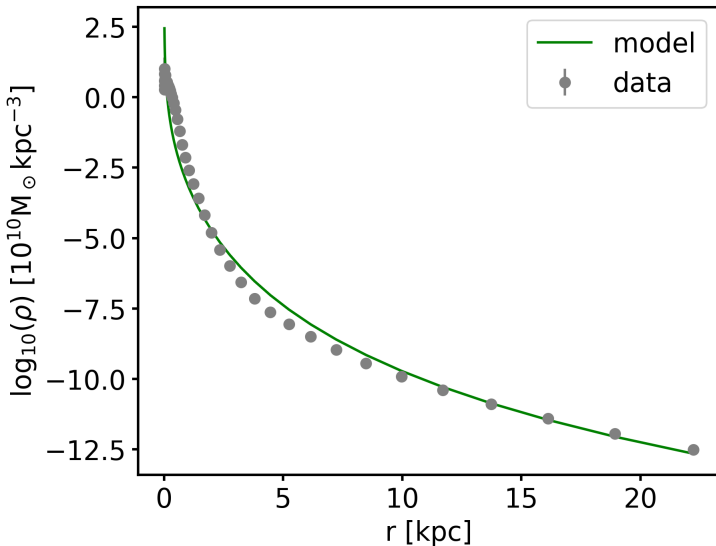


Figure 9: Spheroid density: data with errors (grey dots) and best fit (green line). The data is binned logarithmically in r . Their standard deviation is too small to be seen. In the inner part, $r < 10 \text{ kpc}$, the density is both under and over estimated. In the outer parts, the fit matches the data.

2.2.6 Halo potential

We model the DM halo with a NFW (Navarro *et al.*, 1997) profile following the formula

$$\rho(r) = \frac{\rho_{crit} \cdot \delta_c}{(r/r_s)(1+r/r_s)^2} = \frac{M}{4\pi a^3} \frac{1}{(r/a)(1+r/a)^2} \quad (13)$$

with scale radius $r_s = a$, the critical density $\rho_{crit} = 3H^2/8\pi G$, the mass M of the DM halo and a characteristic and dimensionless density δ_c which can be rewritten as $\rho_{crit} \cdot \delta_c = M/4\pi a^3$. The NFW profile is derived from DMO simulations and found to accurately describe DM halos (Navarro *et al.*, 1997).

All particles in the simulation have a potential value, "pot", which is the potential they feel at their position from the total surrounding matter (not only from the host galaxy). Since the total halo (shown in Figure 3) is isolated and the main matter contribution comes from the main galaxy and its halo, we still consider this a value where we can fit the potential of the analytic model to. We select 100000 DM particles randomly which we present in Figure 10. With the best fit potentials for the stellar components, we set up a potential in galpy with all three components. We need to do this superposition of the potential because fitting a three component potential at once gives us a potential where the halo is overestimated (see Section 2.3). Since we want to fit the DM halo to the potential values provided by the simulation, we need other routines for the stellar components. Therefore, we fit the densities of stellar spheroid and disk. When fitting the total potential, only the NFW parameters are the free ones. We calculate the value of the potential for each of the randomly selected particles in the model and fit these to the true potential with the `scipy.optimize.differential_evolution` routine by minimizing their squared relative errors. The result is shown in Figure 11 where we see the "pot"

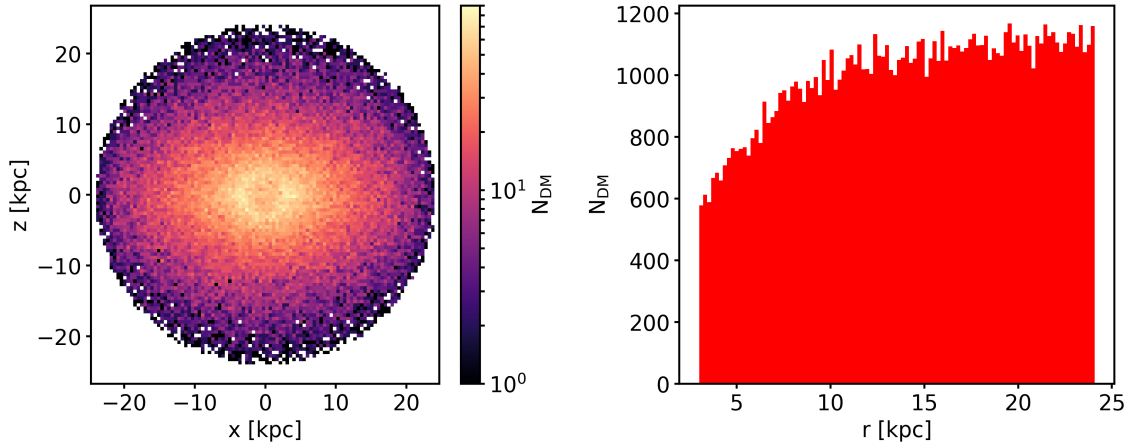
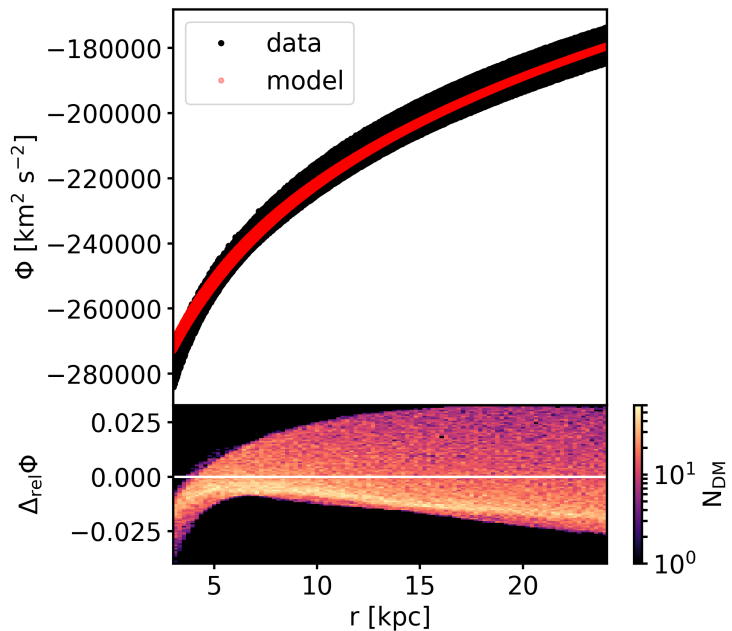


Figure 10: Selection of 100000 random DM particles, used to fit to the NFW halo. *Left panel:* Distribution of particles in the $x - z$ plane. *Right panel:* Number of DM particles depending on r . For $r > 10$ kpc, the distribution is constant while there are less particles for smaller radii. Since we are less interested in the innermost part of the halo, it is good that the weight for the fit lies in the outer parts. DM particles with $r < 3$ kpc are excluded from the fit since it worsened the fit in the outer parts.

Figure 11: *Upper panel:* Potential of data (selected DM particles) and model depending on the radius r . Black dots are data, red dots from the best fit model. The innermost 3 kpc are not included in the fit to make it better in the to us more important outer parts. The model lies everywhere within the data. *Lower panel:* The relative error $\Delta_{\text{rel}}\Phi = (\Phi_{\text{model}} - \Phi_{\text{data}})/\Phi_{\text{data}}$ is within a good range ($< 4\%$).



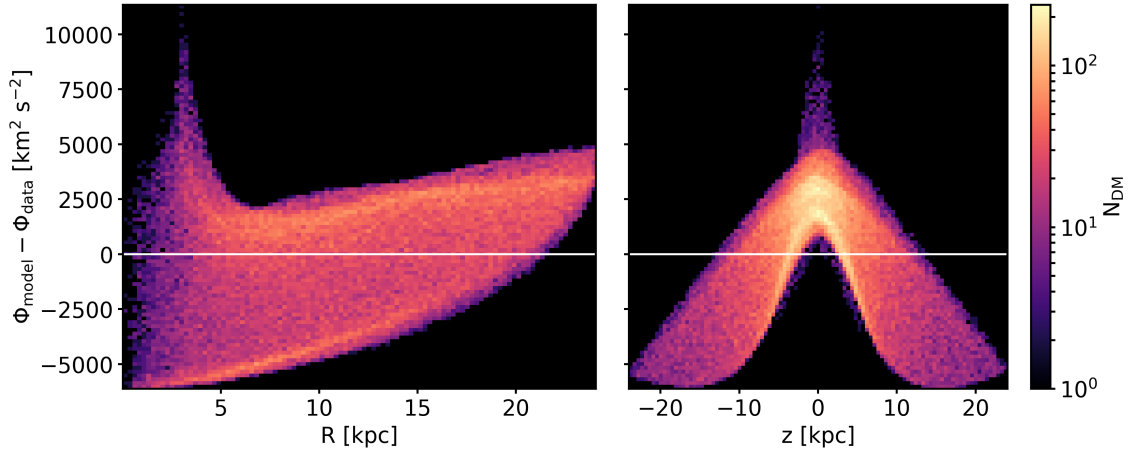


Figure 12: Total error $\Phi_{\text{model}} - \Phi_{\text{data}}$ of the DM fit versus the radius R (*left*) and height z (*right*). While the error in R is still pretty symmetrically distributed around $\Phi_{\text{model}} - \Phi_{\text{data}} = 0$, we see a large systematic error in the disk around $z = 0$.

value of the selected DM particles in black and the fitted NFW potential overlaying in red. Even though the red dots lie within the distribution of the black dots, the slope seems to be different. The absolute errors in Figure 12 reveal more difficulties in the fit of the disk. This might come from the earlier problems in the fits of the stellar disk and spheroid. We discuss this in Section 2.3. However, since the errors are relatively small (within 3-4%) we think the fit is good enough.

We find the best fit scale length of the DM halo, a_{NFWH} as well as the total circular velocity $v_{0,\text{tot}} \equiv v_{\text{circ}}(R_0 = 8 \text{ kpc})$. From that total circular velocity we can subtract the fraction from the stellar components to get the DM component, $v_{0,\text{NFWH}} = \sqrt{v_{0,\text{tot}}^2 - v_{0,\text{MND}}^2 - v_{0,\text{HB}}^2}$. The resulting parameter values are summarized in Table 2.

2.2.7 Total potential

After fitting each component individually, we add them up to get a total potential. In Table 2, we summarize our results for the last snapshot as described in the previous Sections.

To verify the goodness of the total potential, we show the circular velocity curve in Figure 13. The innermost part is underestimated due to an underestimation of the stellar spheroid or disk. The DM proportion in the outer part seems correct. The disk is underestimated due to the sharp decomposition. In overall, the total circular velocity matches the data and the fit in the outer parts, where the particles we investigate in Section 3 are, is reliable.

Table 2: Best fit potential overview: components, used potentials, their parameters with best fit values and their fitting methods.

component	potential	parameters & values	fitting method
stellar disk	Miyamoto -Nagai	$a_{\text{MND}} = 2.97 \text{ kpc}$ $b_{\text{MND}} = 1.64 \text{ kpc}$ $v_{0,\text{MND}} = 105.00 \text{ km s}^{-1}$	MN density fitted to density bins of disk in (R, z) .
stellar spheroid	Hernquist	$a_{\text{HB}} = 1.82 \text{ kpc}$ $v_{0,\text{HB}} = 110.00 \text{ km s}^{-1}$	Hernquist density fitted to density shells of spheroid in (r) .
DM halo	NFW	$a_{\text{NFWH}} = 25.47 \text{ kpc}$ $v_{0,\text{NFWH}} = 160.66 \text{ km s}^{-1}$	Total potential fitted to "pot" value of random DM particles where NFW parameters were fitting parameters.
total	sum of these potentials	$R_0 = 8.00 \text{ kpc}$ $v_{0,\text{tot}} = 221.21 \text{ km s}^{-1}$	v_0 is the total circular velocity at R_0 .

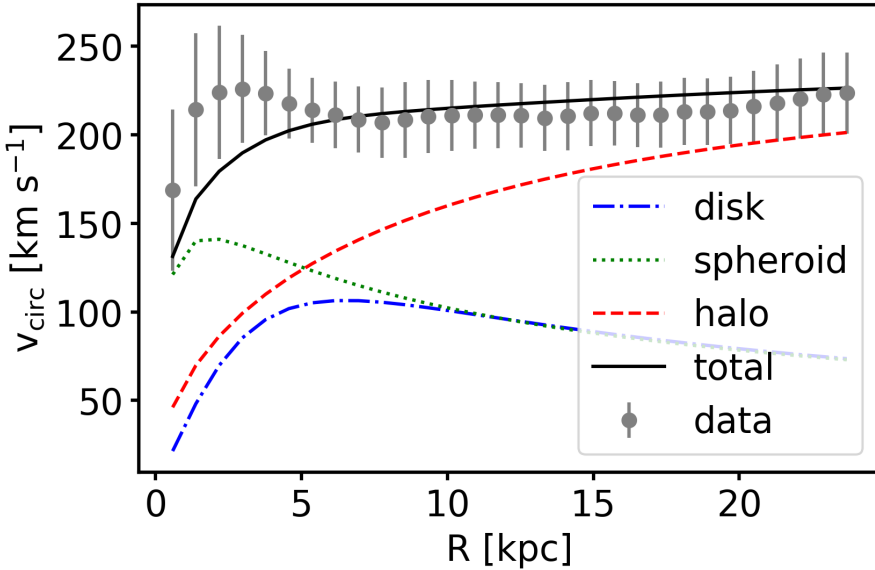


Figure 13: Circular velocity at $z = 0$: data (grey circles), total (black solid line), disk (blue dashed dotted line), bulge (green dotted line) and halo (orange). The data is the mean tangential velocity of all stars which have $\epsilon > 0.95$ and the error is their standard deviation. The model components and the total distribution are calculated analytically. The total curve matches the data within its errors. Disk and spheroid overlay in the outer parts which is due to the decomposition where their proportion is nearly 1 : 1. The DM halo dominates in this parts, as expected. In the center, the circular velocity is underestimated. This is probably due to an underestimation of the spheroid component in the center which we can see find in the density fit in Figure 9. In the outer parts ($R > R_0$), the curves behave as they are expected to do.

Table 3: Comparison of some of the structural parameters of our results with the Auriga (G+17) analysis and MW values taken from Bland-Hawthorn and Gerhard (2016).

Quantity	Unit	This work	Auriga G+17	Milky Way B-H&G16
Disk scale length	[kpc]	2.97	5.57	2.6 ± 0.5 (thin disk)
Bulge scale length	[kpc]	1.82	0.95	$1.9 - 2.8$ VGG09
DM halo scale length	[kpc]	25.47	none	25 ± 10
Disk mass within $0.1R_{200}$	$[10^{10}M_\odot]$	3.15	3.76	3.5 ± 1 (thin disk)
Spheroid / bulge mass within $0.1R_{200}$	$[10^{10}M_\odot]$	3.40	2.19	$1.4 - 1.7$
Total stellar mass within $0.1R_{200}$	$[10^{10}M_\odot]$	6.55	6.55	5 ± 1
D/T		0.47	0.63	0.7 (thin disk)
$R_{200} = R(\rho = 200\rho_{\text{crit}})$	[kpc]	240.86	240.86	209 ± 23
$M_{200} = M(\rho = 200\rho_{\text{crit}})$	$[10^{12}M_\odot]$	1.49	1.49	1.1 ± 0.3
total circular velocity at $R_0 = 8$ kpc	$[\text{km s}^{-1}]$	221.21	none explicitly	238 ± 15

In Table 3, we compare some of our potential quantities to the ones derived in G+17 and to typical MW values. The comparison to the MW is not direct but rather to get an idea of typical quantities of spiral galaxies. Also, different methods and models are applied. However, many of our results are in a similar regime, such as scale lengths and the circular velocity. The difference in our work and in G+17 in masses is due to the decomposition: while G+17 used the first method described in Section 2.2.3 to derive these values, we use the second. The difference in scale lengths is due to different models.

2.2.8 Time evolution

To make sure we can assume a slowly varying potential and to carry out investigations of e.g. the action evolution we need to know the potential for each snapshot. Using the fitting routine described in the previous Sections, we fit a potential to each snapshot individually, without taking the results of the neighbouring snapshots into account, e.g. as a prior. Therefore, the fitting of the time evolution is unbiased in that sense. In Figure 14, we show the time evolution of the potential parameters for the last 10.5 Gyr. In the potential parameters, we see how the galaxy grows and how the growth is affected by mergers. The indicated mergers are described in more detail in the next Section and in Table 4. The overall trend is very smooth and without any outliers. The spheroid's parameters are very constant since the second merger, while the disk and the DM halo are affected by the last merger. While the disk seems to grow in size, its contribution to the total circular velocity decreases. On the contrary, the DM halo contracts but its contribution to the velocity rises more steeply. This shows, that these mergers have a strong impact on the evolution of the potential of this galaxy. Nevertheless, with the interpolation (black line) of the values we still can assume a slowly varying potential which is essential for the action investigations (from Section 3.3 on - see also Section 3.6.1 in Binney and Tremaine, 2008).

2.3 What (not) to do when fitting a gravitational potential to simulations

Even though the total circular velocity of our model matches the data, the single component fits we carry out in Section 2.2 have regions with large errors. We now explain some of the steps we took to develop this algorithm, what did not work and how we can deal with these errors.

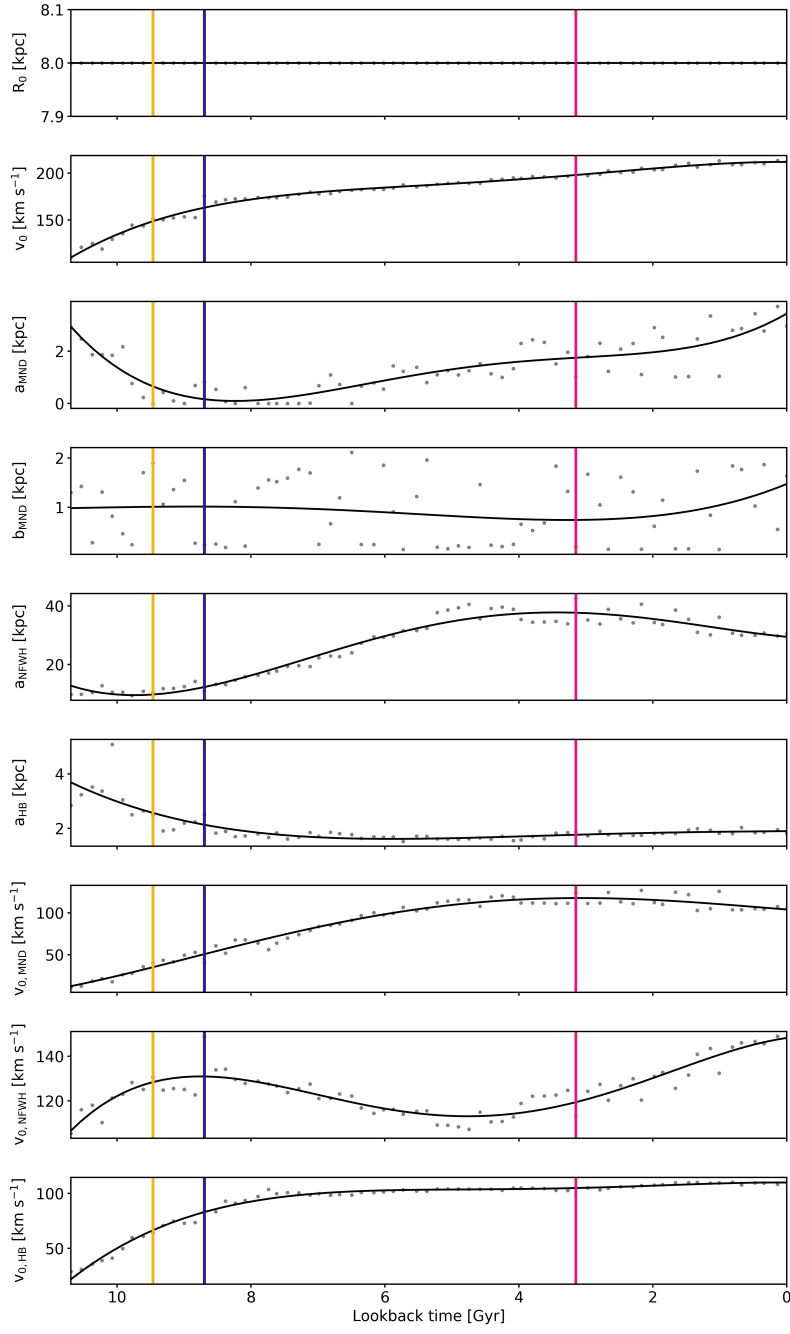


Figure 14: Evolution of all fit parameters over time. $v_0 = v_{\text{circ}}(R_0)$ describes the overall $M(< R_0)$ evolution (see Equation 1) and the other parameters describe scale length - and height, if applicable - and their contribution to the circular velocity at R_0 . The grey dots are the best fit values and the black lines are polynomial fits of 4th order for each parameter. The vertical lines mark the merger times of the three biggest merger events the main halo galaxy has experienced. The pink merger was the latest and biggest merger while the yellow merger contributed the least mass of these. R_0 is kept constant throughout the time evolution to see how within a constant radius the mass changes over time. In the second panel, we see that the mass growth of the galaxy within R_0 is continuous. The second merger flattened out the rise of the total circular velocity which is measured at $R_0 = 8 \text{ kpc}$. More discussion is in the text.

Fit the potential in one step In the first try, we worked with the three component analytic potential as well but we assumed that we can just fit the combined potential to the "pot" value of a different amount of random particles (up to 1 million) of the simulation data. It resulted in a big overestimation of the halo and we had no control in giving each component its proportion.

Decomposition To then fit a potential to each component we carried out a decomposition (Section 2.2.3). This decomposition only takes dynamically cold disk particles into account. We therefore probably underestimated the disk. Doing the decomposition kinematically is a good start but the recipe could be expanded by some more complex disk characteristics, e.g. different or more flexible models beyond the MN-family. To get around the decomposition one could try to fit all stellar particles to a combination of disk and spheroid potentials.

Binning and weighting of the data Once we made a selection of disk and spheroid particles, we had to bin our densities to fit models to them. Depending on bin distances (e.g. linear or logarithmic bin edges), sizes and weights, the focus of the fit is given to particular regions of the data. This has to be taken into account when preparing the data to be fitted.

Fitting routines There are many methods of fitting models to data and these different methods offer a wide range of different implementations. We tried several for the different components. The first we used was `scipy.optimize.minimize` looking for the minimum of the relative error between data and model. This fitting routine finds local minima. Therefore it sometimes ran into very unphysical parameters and found them to be the best fit. This routine was therefore too simple. We tried fitting the parameters with a MCMC algorithm, `emcee` (Foreman-Mackey *et al.*, 2013), but this did not always converge so it was also not the best choice for us. Another `scipy.optimize` routine is `differential_evolution` which finds the global minimum. So here again we minimized the relative error. This worked on the 1D models in the spherical potentials and we used it for the halo potential. It did not fit the 2D MN potential as the algorithm just tried to set the model to 0 which would give in a small relative error but it resulted in extremely flat and elongated disks ($a_{\text{MND}} = \text{upper boundary}$ and $b_{\text{MND}} = 0$). The last fitting routine we then used on the MN disk was `scipy.optimize.curve_fit` which fits absolute differences between data and model but only requires the binned density and the model as input without the need to define how it minimizes the problem. This then worked for the disk the best. We also used it to fit the stellar spheroid density in logarithmic bins $\log(\rho)$ and $\log(r)$ rather than in ρ over r .

Find proper fitting characteristics We fitted the stellar components to the stel-

lar densities and the DM profile to the potential value. In addition, we could also consider fitting all three components in addition to their circular velocities. This would give us a constraint from the dynamical side and could make the fit better.

To fit an analytic axisymmetric potential to a hydrodynamical galaxy simulation is not easy and requires some assumptions. We have some problems, i.e. with the fits in the disk. Still, the circular velocity curve of our model matches the data (Figure 13) reasonably well. We are confident that this potential fit is good enough to carry out further investigations in this model but we also want to emphasize that there is still room for improvement

3 Adaptive dynamics: Can actions of accreted globular clusters constrain the gravitational potential?

3.1 Integrals of motion

This Section is based on §3.1, §3.2 and §3.5 of Binney and Tremaine (2008). Objects (e.g., stars and GCs) in a gravitational potential move on orbits which are described by their positions and velocities in 6 dimensional phase space, (\mathbf{x}, \mathbf{v}) . Functions I , which are constant along an orbit, are called integrals of motion (IoMs) (Binney and Tremaine, 2008):

$$I[\mathbf{x}(t_1), \mathbf{v}(t_1)] = I[\mathbf{x}(t_2), \mathbf{v}(t_2)] \quad (14)$$

for any t_1 and t_2 . This means, that the time derivative of these IoMs is 0:

$$0 = \dot{I}. \quad (15)$$

In an axisymmetric 3D potential as we assumed and fitted in Section 2 orbits can have up to three IoMs.

3.1.1 Energy and angular momentum

Energy E and some components of the angular momentum \mathbf{L} , depending on the symmetry of the potential, are regarded as classical IoMs. In a spherical potential, all three components of $\mathbf{L} = \mathbf{x} \times \mathbf{v}$ are IoMs while in the axisymmetric potential Φ , the only component of the angular momentum which is an integral of motion is L_z , i.e. the component aligned with the symmetry. The energy is given by the Hamiltonian H ,

$$H(\mathbf{x}, \mathbf{v}) = \frac{1}{2}v^2 + \Phi(\mathbf{x}) = E \quad (16)$$

with the total velocity v . In an axisymmetric potential, the IoMs (E, L_z) are supplemented by a third integral of motion, $I_3 = \text{constant}$, which, in general, does not have an analytic expression and therefore is a non-classical integral.

3.1.2 Actions

General introduction to actions A particular set of IoMs are actions which, together with angles, create a canonical coordinate system. These actions are three momenta, $\mathbf{J} = (J_1, J_2, J_3)$, which describe the whole orbit while the angles, $\boldsymbol{\theta} = (\theta_1, \theta_2, \theta_3)$ define the position of the object on the orbit. Orbits for which actions can be calculated are called regular orbits. The three actions are given by the integral

$$J_i = \frac{1}{2\pi} \oint_{\gamma_i} \mathbf{p} \cdot d\mathbf{q} \quad i = 1, 2, 3 \quad (17)$$

over the path γ_i with vector $\mathbf{q}(t)$ and corresponding momentum $\mathbf{p}(t)$ given a Hamiltonian system which satisfies

$$\dot{\mathbf{q}} = \frac{\partial H}{\partial \mathbf{p}} \quad ; \quad \dot{\mathbf{p}} = -\frac{\partial H}{\partial \mathbf{q}}. \quad (18)$$

The range of the angles is by construction $\theta_i = [0, 2\pi]$ so that it moves periodically around the center of the galaxy. Since $0 = \dot{J}_i = -\partial H / \partial \theta_i$ (Equation 15), the Hamiltonian is independent of $\boldsymbol{\theta}$. Therefore, angles follow the time evolution

$$\dot{\theta}_i = \frac{\partial H}{\partial J_i} \equiv \Omega_i(\mathbf{J}), \quad \text{a constant} \quad \Rightarrow \quad \theta_i(t) = \theta_i(0) + \Omega_i t \quad (19)$$

with the fundamental frequencies Ω_i . The components of $\boldsymbol{\theta}$ evolve linearly in time.

Definition in cylindrical coordinates In the axisymmetric potential, we have the spatial coordinates (R, ϕ, z) and velocities (v_R, v_ϕ, v_z) which we can use for the planes (x_i, v_i) in which we examine the actions $\mathbf{J} = (J_R, J_\phi = L_z, J_z)$. The actions quantify the oscillation of the orbit in the given coordinate direction. J_R describes how the object moves towards and away from the galactic center, the radial oscillation. J_z quantifies the oscillation above and below the equatorial plane while $J_\phi = L_z$ is the angular momentum along the symmetry axis. Circular orbits do not oscillate in R and z so the actions in these directions are $(J_R, J_z) = 0$.

Numerical calculation of actions Only in a simple spherical symmetric potential, the Isochrone potential $\Phi(r) = -GM/(b + \sqrt{b^2 + r^2})$ with scale length b , actions can be calculated analytically without a single integration. To numerically calculate the actions of objects in our axisymmetric potential from Section 2, we need to use approximations. With the motions (u, v) defined by

$$R = \Delta \sinh u \sin v \quad ; \quad z = \Delta \cosh u \cos v \quad (20)$$

3.2. Globular cluster sample selection

and their canonical conjugate momenta $p_u(u, E, L_z, I_3)$ and $p_v(v, E, L_z, I_3)$ we can transform the Hamiltonian:

$$H(R, z, p_R, p_z) \Rightarrow H(u, v, p_u, p_v). \quad (21)$$

Under the assumption of *separable* Stäckel potentials (de Zeeuw, 1985) which have the form

$$\Phi(u, v) = \frac{U(u) - V(v)}{\sinh^2 u + \sin^2 v} \quad (22)$$

we can solve the Hamilton-Jacobi equation by the *separation of variables* ansatz to decouple the motions in u and v . Then, both sides of the equation are constant. By clever choice, this constant depends on the third integral of motion, I_3 and on the focal length Δ which defines the coordinate system. The resulting actions J_u and J_v depend on the three computable actions (E, L_z, I_3) , the focal length Δ and on the Stäckel potential but need only one integral to solve instead of an orbit integration. The cylindrical actions are $J_R \approx J_u$ and $J_z \approx J_v$. The Stäckel Fudge method (Binney, 2012a; Bovy and Rix, 2013), just pretends that the given potential is a Stäckel potential. The closer the potential is to a Stäckel potential, the better it will work. A more formal introduction is given in Binney and Tremaine (2008); Binney (2012a); Bovy and Rix (2013) and in Trick (2017).

This algorithm is implemented in `galpy` with the need of the focal length Δ and we use it for the action calculations where we calculate Δ for each potential to keep numerical caveats as small as possible.

3.2 Globular cluster sample selection

Due to the resolution of the simulation, $M = 5 \cdot 10^4 M_\odot$, we set one stellar particle as one GC. All stellar particles which were accreted by the main halo are followed through the evolution and kept as accreted GCs as long as they do not cross the disk in a sense that they are directly in the disk - defined empirically per snapshot as within the disk radius $R_d = 0.05R_{200} \approx 12$ kpc and the height $z_d = 0.06 R_d \approx 0.7$ kpc - to match the MW disk's scale height in the $z = 0$ snapshot - since we assume that in that case the GC would be disrupted (Aguilar *et al.*, 1988; Moreno *et al.*, 2014).

We select the three merger events and present their properties in Table 4. We select the biggest mergers since in an external galaxy we want to distinguish the GCs by their AMR. The bigger the DG, the more GCs are accreted and the better we can distinguish merger events and their GCs. Our sample size (Column 3 in Table 4) is not physically motivated but only selected from a very simple cut and therefore too big. However, this should not affect our results. We discuss this in Section 4.

Table 4: Progenitor parameters. The selected progenitors are the same as in Figure 15.

name	merger time [Gyr]	number of accreted particles	total mass of accreted particles [$10^8 M_\odot$]	mass of main galaxy at merger [$10^{10} M_\odot$]	remnants to galaxy ratio
prog2	3.15	24793	9.2	5.93	0.016
prog3	8.70	22079	8.3	2.28	0.036
prog4	9.46	6511	2.5	0.74	0.034

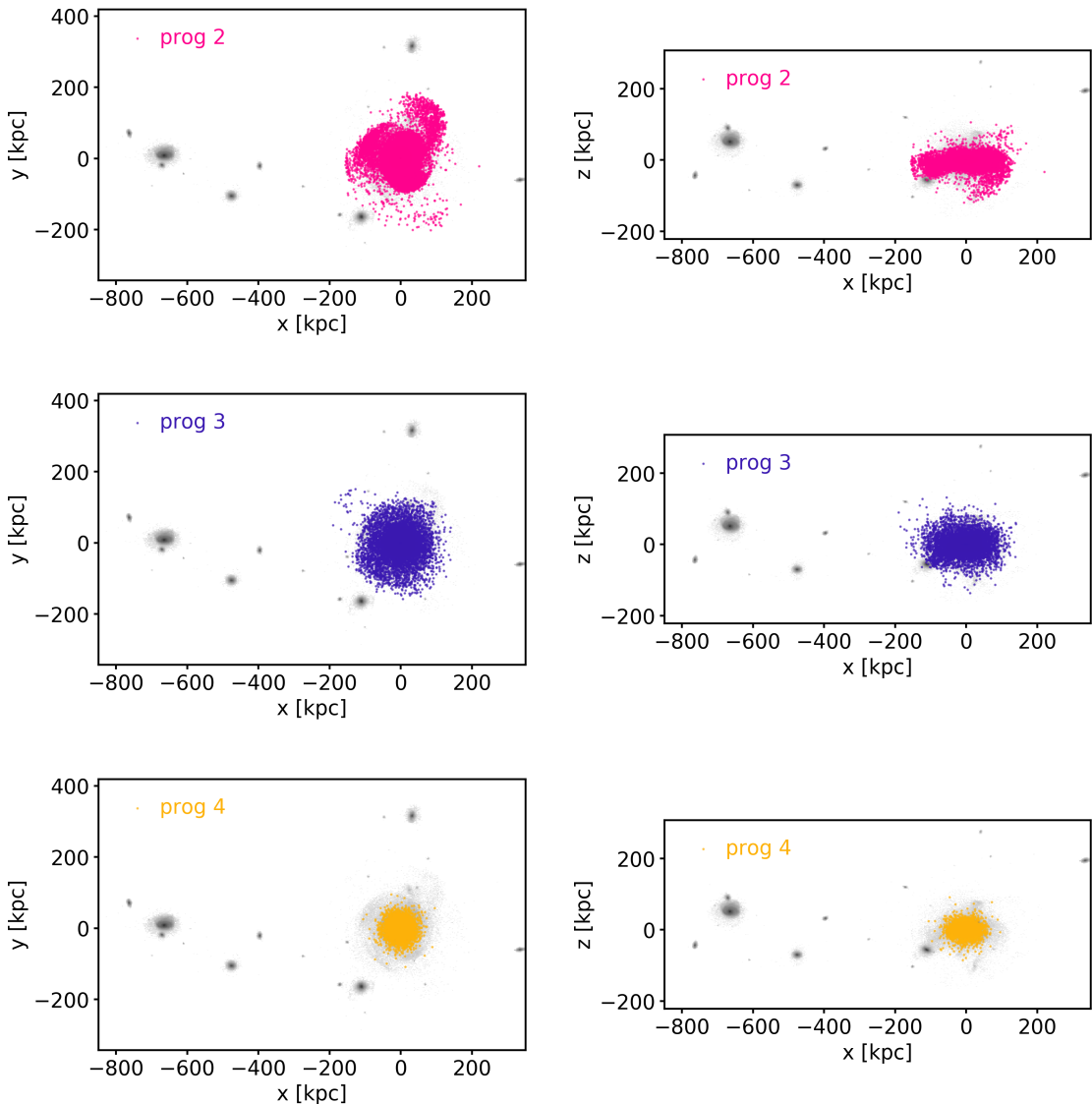


Figure 15: Remnants of the three biggest DG mergers which were not destroyed by the disk. The left panels show the $x - y$ distribution, the right panels the $x - z$ distribution. In grey, the main galaxy and its satellites are plotted (as in Figure 3). *Upper panels:* The remnants of the most recent merger are plotted in pink. *Middle panel:* The blue points are remnants of the second biggest merger. *Lower panel:* The yellow points are remnants of the third biggest merger which is the most long ago of these three. These remnants will be considered the GC populations of each merger event.

The positions of the remnants of these three merger events are shown in Figure 15. Prog3 and prog4 are totally dispersed in the galaxy while prog2 still shows some merging features such as broad streams, especially visible face-on.

3.3 Globular clusters in action space

Now, we look at the GC distribution in action space. Our assumption is that in the "true" potential, GCs are very clumped since they should retain dynamical memory from their former DG's orbit and therefore their DF should be a δ -function. In Section 3.3.1, we will look at the distribution in the fitted potential at redshift 0. In Section 3.3.2, we evaluate actions in varying potentials to test our assumption of GCs being most clumped in action space in the "true" potential.

3.3.1 Best fit potential

We calculate the actions of the remnants of each progenitor in the best fit potential from the coordinates $(R, \phi, z, v_R, v_\phi, v_z)$ at $z=0$ and plot them in Figure 16. The most recent remnant, prog2, is most distinguishable in L_z . It is corotating with the disk but with higher angular momentum. Prog3 and prog4 are not rotating. In the vertical action, the three remnant groups are not distinguishable and have means close to 0 kpc km s^{-1} . In J_R , the groups are again distinguishable since prog2 has a mean $J_R = 0 \text{ kpc km s}^{-1}$ while the older remnants have a higher radial oscillation. Prog2 seems to have merged in the disk plane while prog3 and prog4 have dispersed more spherically. We can see this spatial distribution in Figure 15 where we also notice that prog2 has not fully merged yet.

The idea of this method is that in the right potential, these groups minimize their spread in action space. Prog4 is the most compact group, while especially prog3 is very dispersed. None of the distributions looks like a δ -function. To quantify the compactness, we measure the standard deviation of each action. In the next Section, we compare the standard deviations of the radial and vertical actions of each group in different potentials to see, if we minimize them in the "true" potential.

3.3.2 Varying potentials

The GCs are at distances where the potential is dominated by the DM halo (see Figure 13). Variations in that component should have the biggest impact on their action space distributions. Therefore, we vary the DM halo by keeping all best fit potential parameters constant and only vary the scale length a_{NFW} . For the three

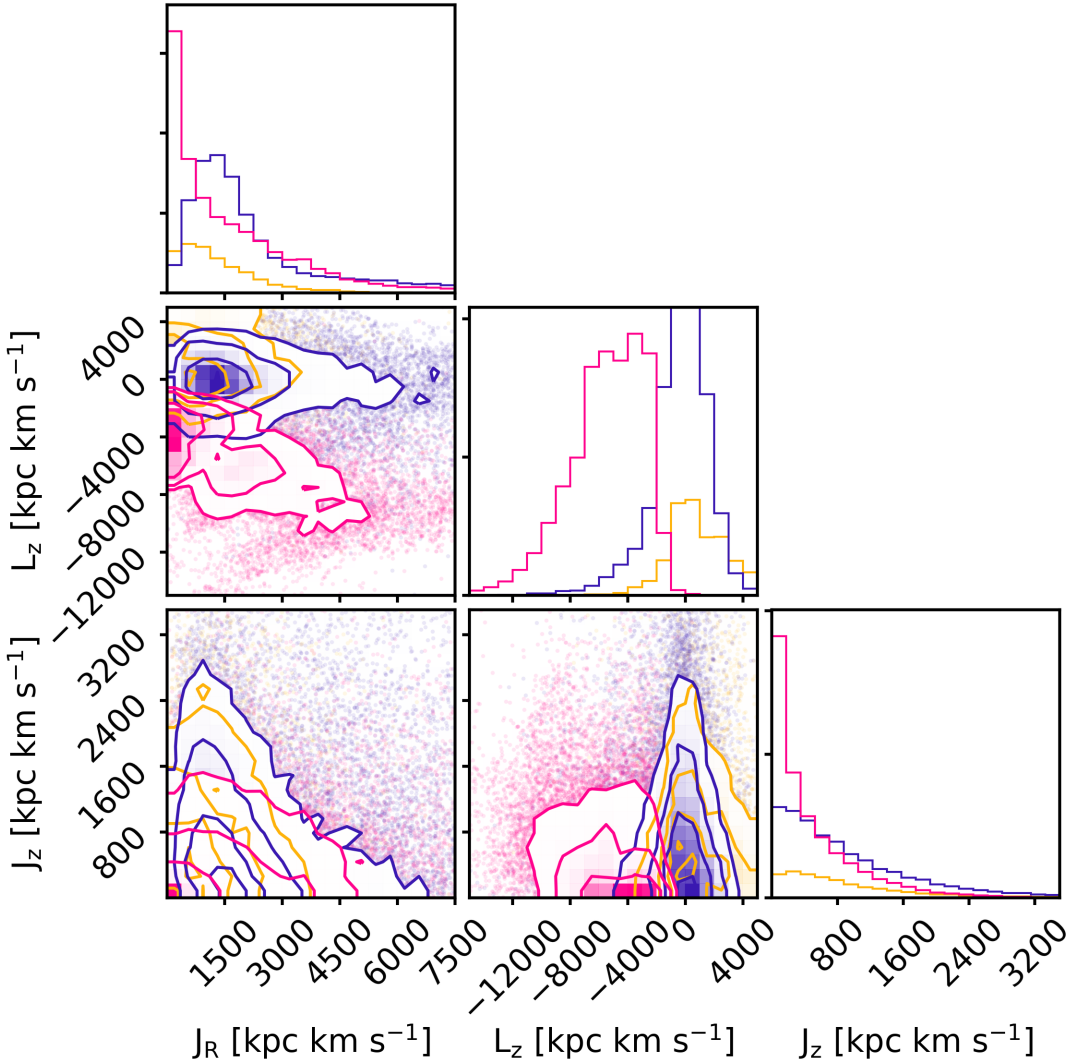


Figure 16: Selected GCs from three different DGs in action space. The diagonal elements show histograms of each action and the other panels show 2D histograms of each action pair. In pink/blue/yellow, we see the action distribution of the remnants of prog2/prog3/prog4. Prog2 and prog3 have more particles than prog4 and therefore dominate the 1D histograms in the diagonal elements. In the correlation panels, we can clearly distinguish prog2 in L_z and J_R while prog3 and prog4 distribute around the same means. The distribution of prog2 is broad in L_z and more narrow in $J_R - J_z$. prog2 is corotating with the disk but with a higher angular momentum than the disk has ($\bar{L}_z = -2235 \text{ kpc km s}^{-1}$). prog3 and prog4 have a mean angular momentum of 0 and mean higher radial action than prog2. Their motion seems to be independent of the disk. All groups have rather broad distributions in the actions.

3.4. Time evolution of actions

groups in these potentials, we calculate the actions in the $z = 0$ snapshot.

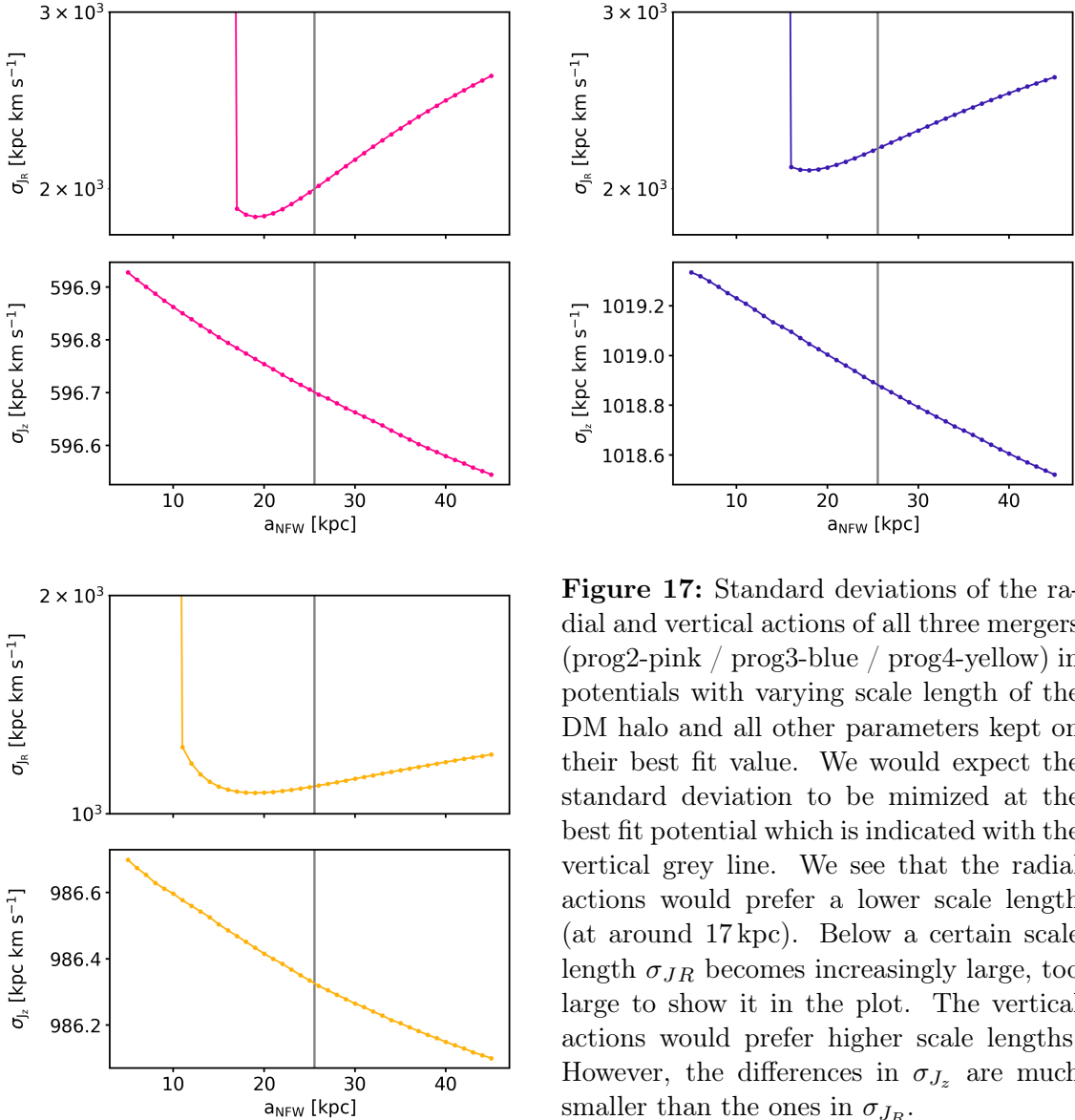


Figure 17: Standard deviations of the radial and vertical actions of all three mergers (prog2-pink / prog3-blue / prog4-yellow) in potentials with varying scale length of the DM halo and all other parameters kept on their best fit value. We would expect the standard deviation to be minimized at the best fit potential which is indicated with the vertical grey line. We see that the radial actions would prefer a lower scale length (at around 17 kpc). Below a certain scale length σ_{JR} becomes increasingly large, too large to show it in the plot. The vertical actions would prefer higher scale lengths. However, the differences in σ_{J_z} are much smaller than the ones in σ_{JR} .

In Figure 17, we see how the standard deviations of the radial and vertical actions evolve in the different potentials. For all three GC groups we see that in the radial action they would prefer a smaller scale length than the true value of the halo potential. The changes in vertical action are smaller but all three groups would prefer a larger scale length than the true one.

This leads us to the conclusion that in the "true" potential, accreted GCs of one DG are not on similar orbits but have a DF that is more complex. We cannot constrain an analytic axisymmetric gravitational potential by only minimizing the spread of these GCs in action space.

3.4 Time evolution of actions

We evaluate the time evolution of the orbits of the accreted GCs to see if there was a point - probably shortly after their mergers - where the GCs were more clumped in action space and the DF could have been a δ -function. If that would be true, we could at least determine the potential of external galaxies which are in a state shortly after a minor merger. We calculate the actions of the selected particles in the best fit potential in each snapshot.

3.4.1 Best fit potential

With the method described in Section 2.2 we fit an analytic axisymmetric potential to each snapshot individually and interpolate the parameters for a smooth potential evolution (see Figure 14). We trace back the GCs we considered as merged and calculate their actions in each snapshot for both after and before the merger.

In Figures 18, 19 and 20 we present these time evolutions for the GCs of prog2 / prog3 / prog4, respectively. For the prog2 GCs, Figure 18, we see nicely how before the merger the actions were very widely spread and towards the merger and especially afterwards their variance becomes smaller and the mean of each action stays constant. Since the merger, more significant clumping than in the last snapshot is not seen. In prog3, Figure 19, we find a large overdensity shortly after the merger. The actions of prog4, Figure 20, are strongly varying shortly after the merger for about 2 Gyr before they become steady.

3.4.2 Mean best fit potential

The idea that actions do not change over time is valid in a static or only slowly varying (axisymmetric) potential. Even though the overall action distribution did not change too much over time, we will see in Section 3.5 that individual orbits vary drastically over time. Therefore, we need to test if the assumption of having a potential which only varies slowly is true. A rather simple execution is to calculate the action evolution in a static potential and check if it varies from our results. To do so, we calculate the mean of each potential parameter since the last big merger event (prog2).

In Figure 21, we show again the parameter evolution and the mean value for each which we use to set up the static gravitational potential. Since we have large scatter in the disk and halo parameters it is interesting to see if ignoring their variation has any consequences on the action calculation. In the time regime since the last merger

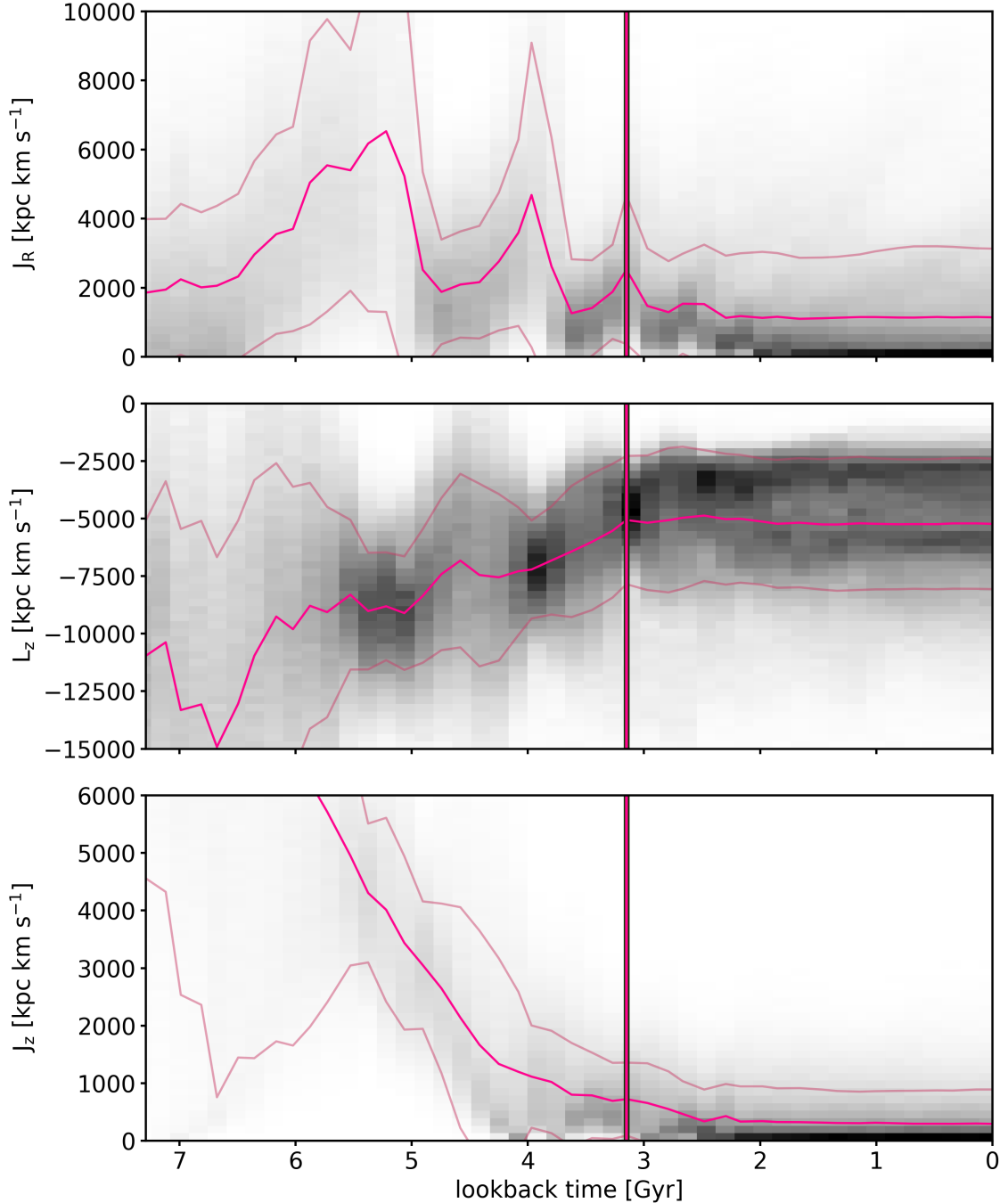


Figure 18: Evolution of actions of prog2 GCs over time. The pink vertical line indicates the time of the merger. The other pink lines follow the median (bright pink) and the standard deviation (light pink). *Upper panel:* Radial action. *Middle panel:* Angular momentum. *Lower panel:* Vertical action. Before the merger, the vertical actions were much higher and all three actions had higher standard deviations. This indicates that their motions were not yet governed by our main galaxy's potential. With the merger, they have settled and all of them have a constant mean and standard deviation since < 1 Gyr after the merger.

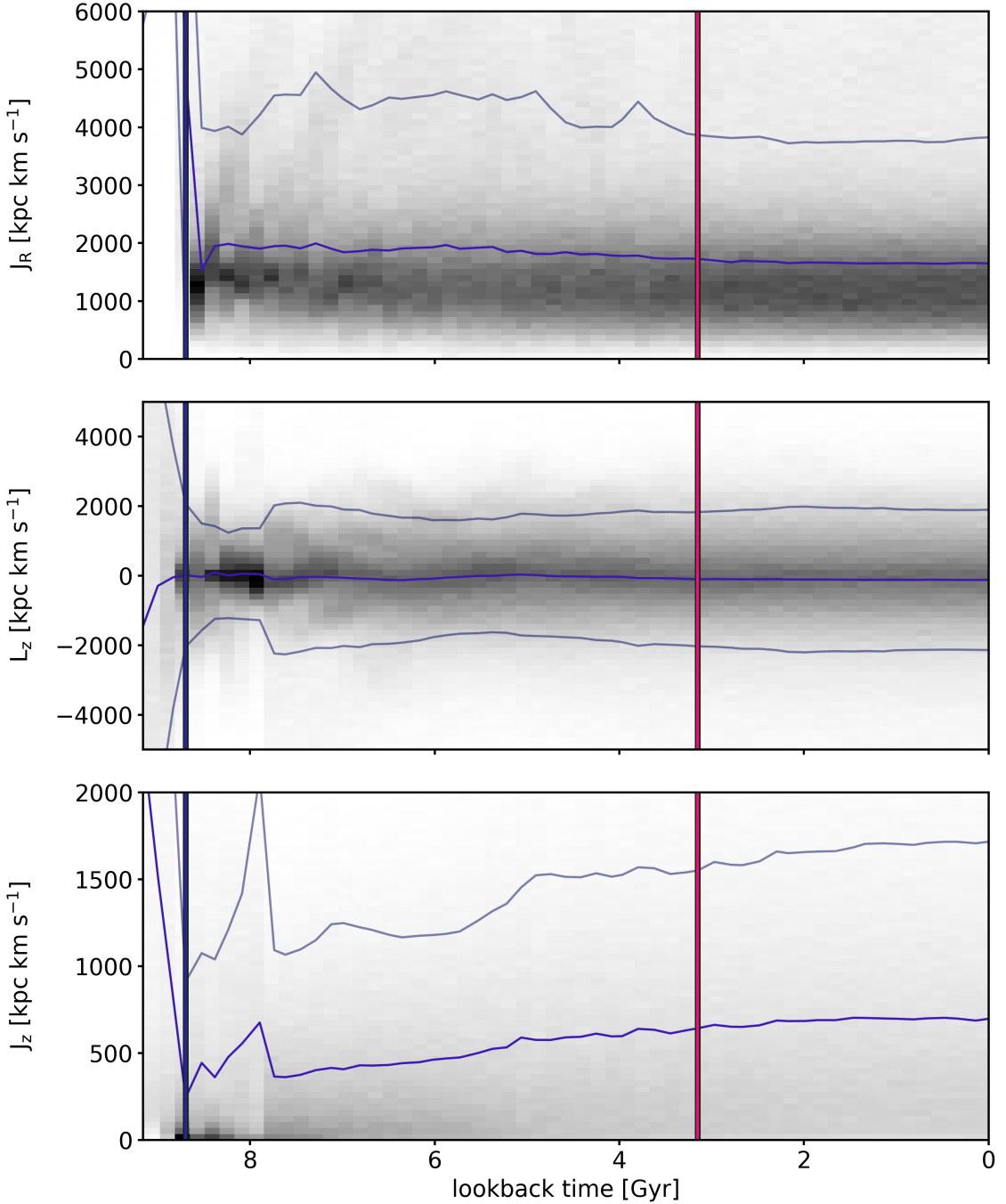


Figure 19: Time evolution of actions of prog3. The vertical pink and blue lines indicate times of the mergers of prog2 and prog3, respectively. The other blue lines are the median and the standard deviation. The panels are the same as in Figure 18. During the merger of prog3, \bar{J}_z and σ_{J_z} minimize. At that time, disk and halo parameters of the potential change slopes (see Figure 14), probably caused by this merger. Shortly after the merger, the spread in J_R and in L_z minimizes while at the same time the median of J_z and σ_{J_z} rise steeply. The following evolution is rather constant for all actions with the spread slowly increasing.

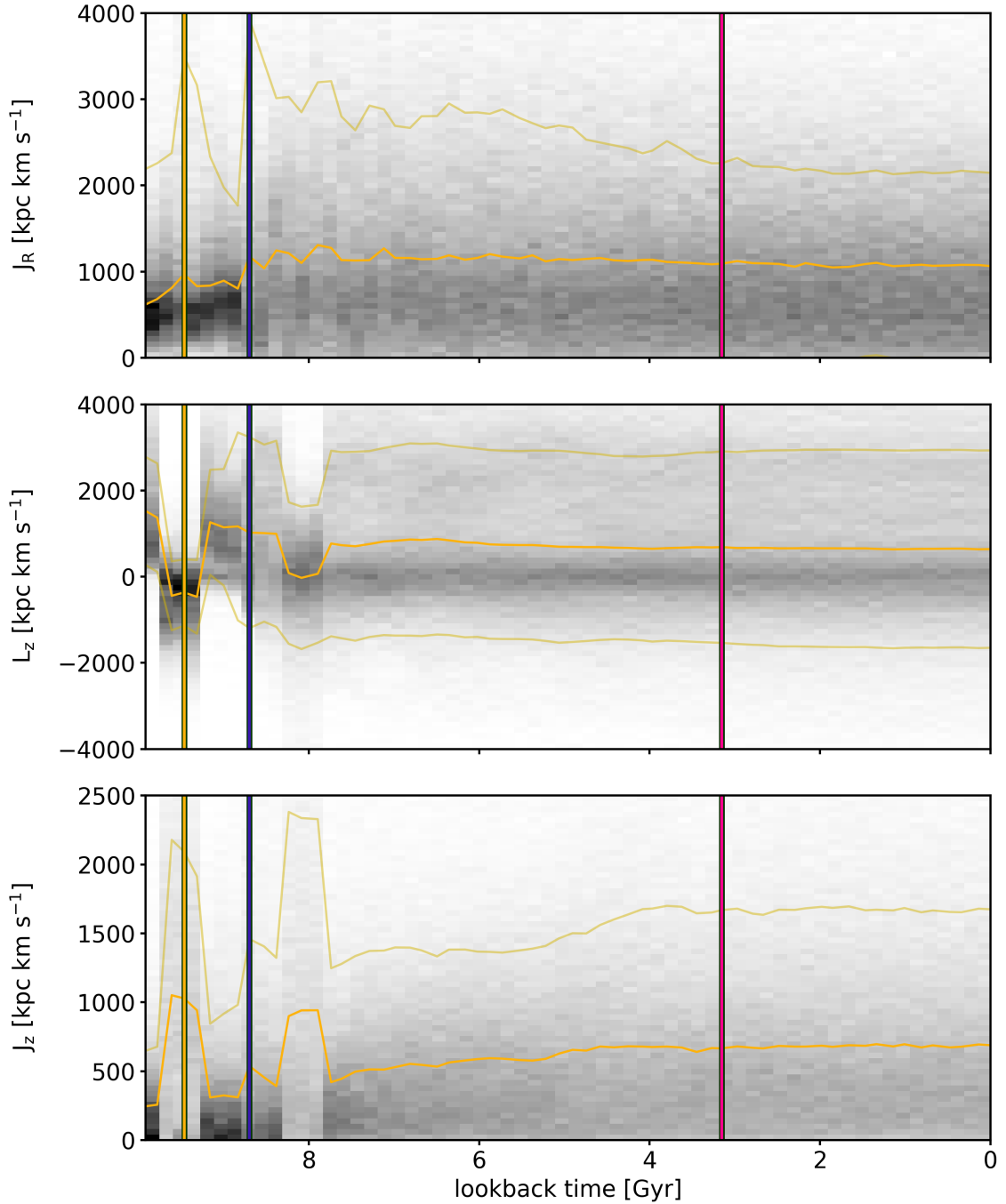


Figure 20: Prog4’s GCs time evolution in action space. The vertical pink, blue and yellow lines indicate times of the mergers of prog2, prog3 and prog4, respectively. The yellow lines are median and standard deviation. The panels are the same as in Figure 18. During the merger of prog4, radial and vertical actions have a steep rise while L_z drops below 0. Something similar happens shortly after the merger of prog3. Since 7.5 Gyr the actions stay constant and with the merger of prog2, the scatter in J_R and J_z becomes even less, is, however, still very large.

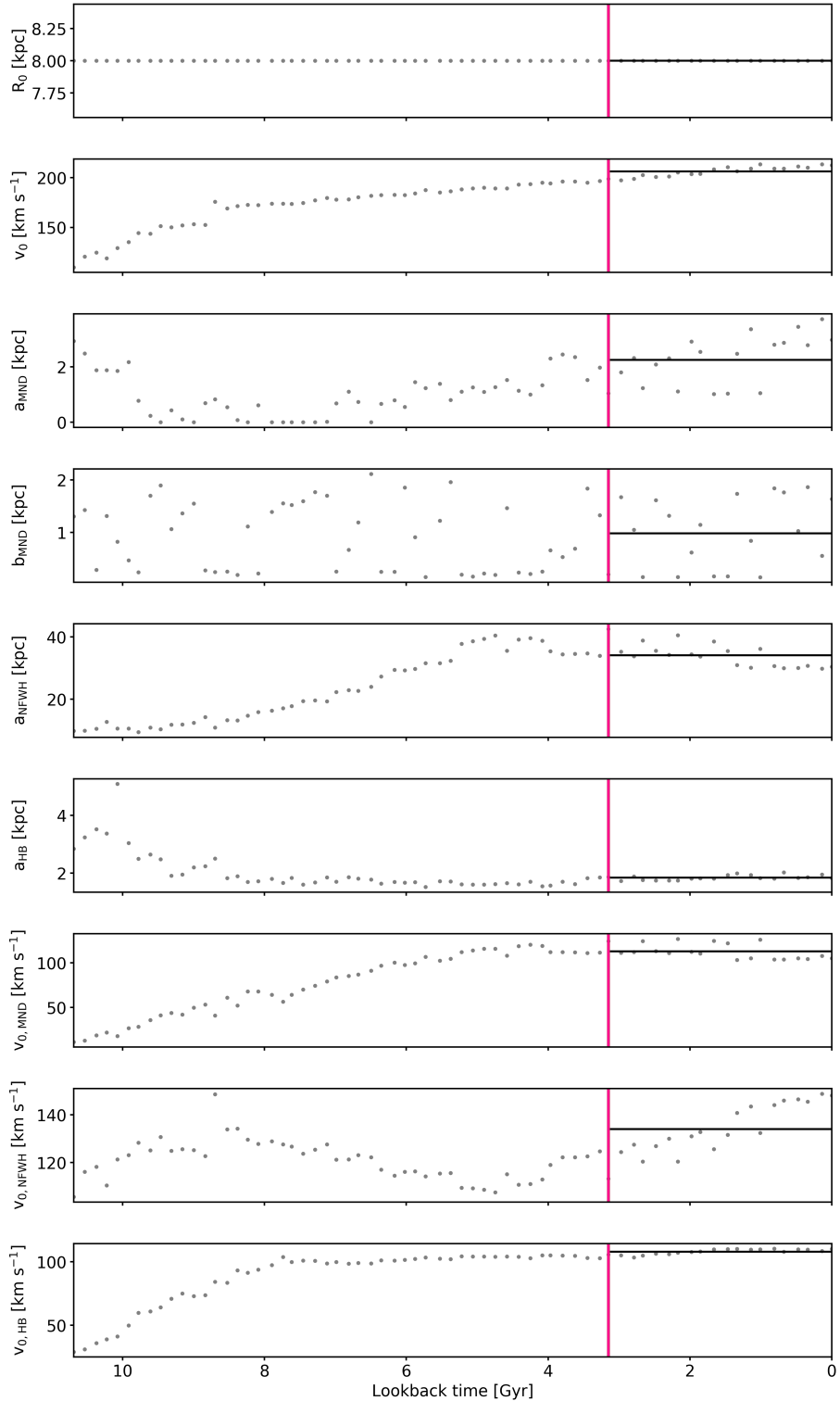


Figure 21: Time evolution of best fit potential parameters and their mean values since the merger of prog2 (indicated in pink). The scatter of disk and halo parameters is relatively large while the bulge parameters stay constant in this time range. We use the mean potential parameters (indicated as black lines) to compare the actions in the slowly varying potential (Figure 14) to the actions in this static potential.

3.4. Time evolution of actions

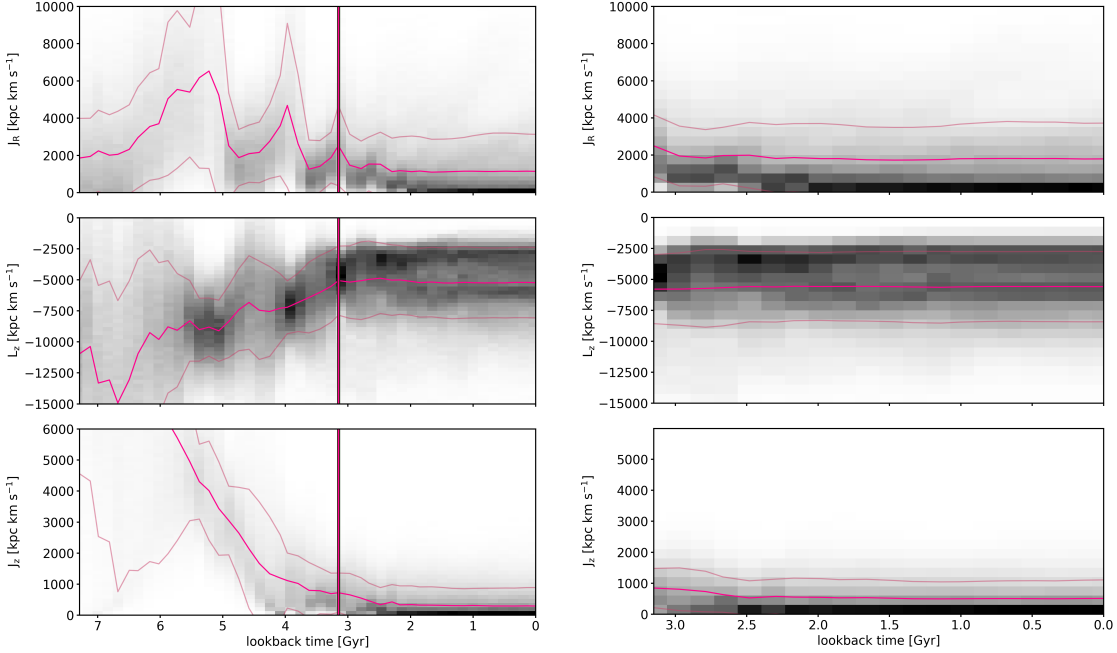


Figure 22: Action evolution of prog2. *Left panel:* same as Figure 18. *Right panel:* Action evolution of prog2 since its merger in a constant potential with parameters given in Figure 21. \bar{J}_R and \bar{J}_z are slightly larger in the constant potential. The standard deviations and the slopes of the evolution stay the same.

we calculate the actions of each progenitor group in the static potential. In Figure 22, we compare the GCs of prog2 in action space in the varying potential (*left*) and the static potential (*right*). There is no difference in the time evolution visible after the merger. We did the same for the GCs of prog3 and prog4 and they also show no differences. Therefore, the assumption of having a slowly evolving potential can be considered as satisfied.

3.4.3 Energy evolution

Another assumption under which we calculated the radial and vertical actions were the use of the action estimation method "Stäckel Fudge". To test if variations and the missing of clumpiness could be due to estimation inaccuracies or numerical problems in this approach we can have a look at the other IoMs, angular momentum and energy. Since L_z was rather constant in Figures 18 - 20 and 22 we now evaluate the energy. It is calculated according to Equation 16 where $v^2 = \sum_{i=1}^3 v_i^2$. We can derive the energy directly from the data by taking the potential value from the simulation. We also compare it to our potential model. The kinematic term of Equation 16 is identical for data and model.

We show the energy evolution in Figure 23. Here it again becomes obvious, that the potential fit could be better since the model underestimates the energy up to a

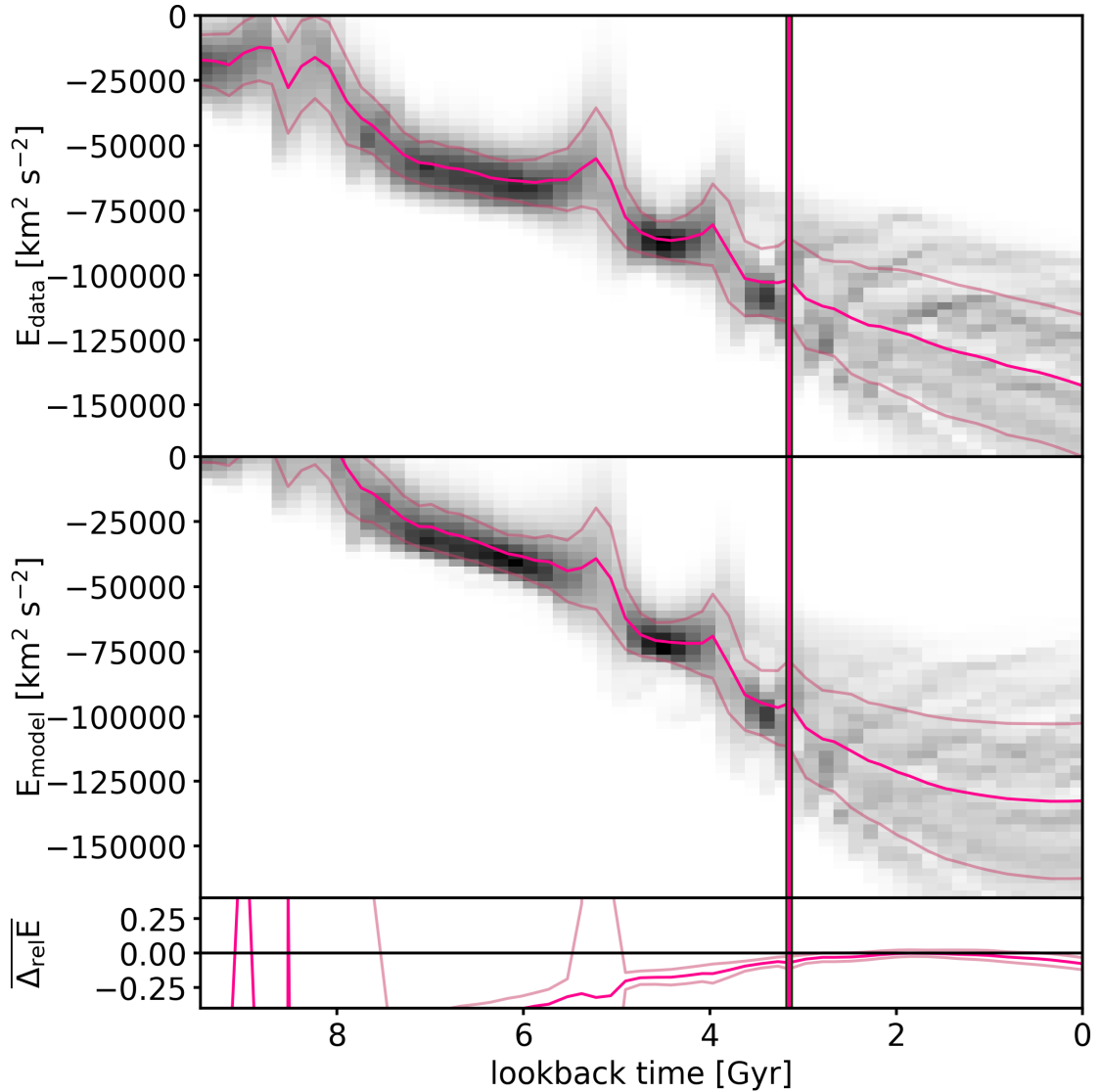


Figure 23: Time evolution of the energy of the particles of prog2. The vertical pink line indicates the merger. The other pink lines are mean and standard deviation. *Upper panel:* The true energy, which the particles have according to their kinetic energy and their potential value as returned by the Auriga simulation. *Middle panel:* Energy calculated in the interpolated best fit potential. *Lower panel:* Mean relative error of the energy, $\Delta_{\text{rel}}E = (E_{\text{model}} - E_{\text{data}})/E_{\text{data}}$. The GCs spiral in and continue to lose energy even after the merger with some small scale variations. The error becomes smaller after the merger.

few $10\,000 \text{ km}^2 \text{ s}^{-2}$. Especially before the merger, the relative error is very big (too big to display it). As the GCs spiral in, the relative error becomes smaller. It seems like the potential fit got better there. Apart from the errors, the overall trend is similar for model and data. As the DG spirals in it falls deeper into the potential well. This trend continues even after the merger. Therefore it still loses energy. We find the same trend for prog3 and prog4. We observe small scale variations in the energy, similarly to what is seen in the actions (best seen in J_z in Figure 19). This results supports the conclusion that our algorithm in modelling the galaxy is good enough but the galaxy is too complex to simply assume the DF of accreted GCs in action space as δ -function.

3.5 Test: evolution of globular clusters on same orbit at $z = 0$

In Section 3.3 we found that the overall GC distribution in action space is not very clumped. In Section 3.4 we saw a rather constant evolution of the actions but with a large scatter. Now we investigate GCs whose actions are close together in the last snapshot. The selection of these "box GCs" is made by taking the mean of each action and find all GCs within a cube centered on the means with a gradually increasing side length. For prog2, we want to look at a larger of 20 particles. To have 20 particles in this cube required a side length of $250 \text{ kpc km s}^{-1}$.

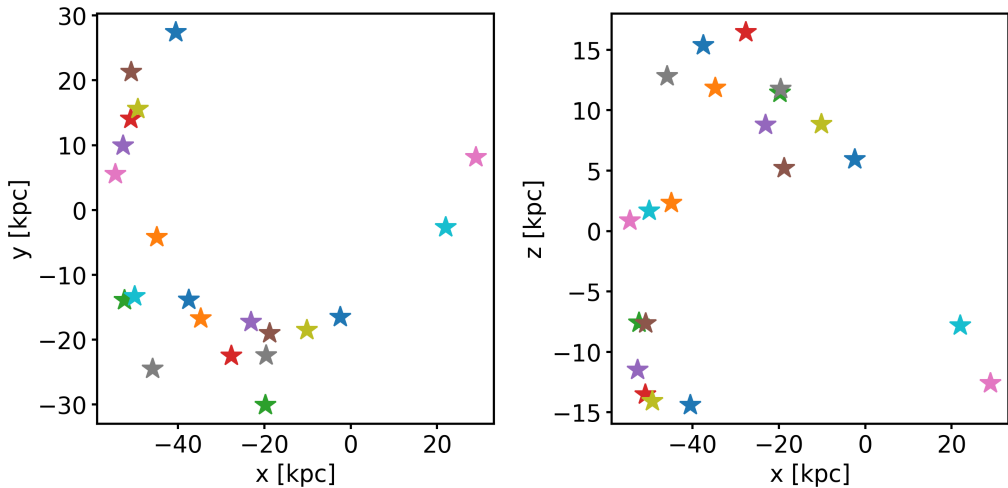


Figure 24: Spatial distribution of selected box particles of prog2. There is a small clustering - red, violet and yellow GCs - visible at $x \approx -50 \text{ kpc}$. All other GCs are well distributed in space.

Their spatial distribution is presented in Figure 24. There is a small clustering around $x = 50 \text{ kpc}$ but all other selected GCs are well distributed in space.

In Figure 25, we plot the evolution of these actions in the right panel. At the last

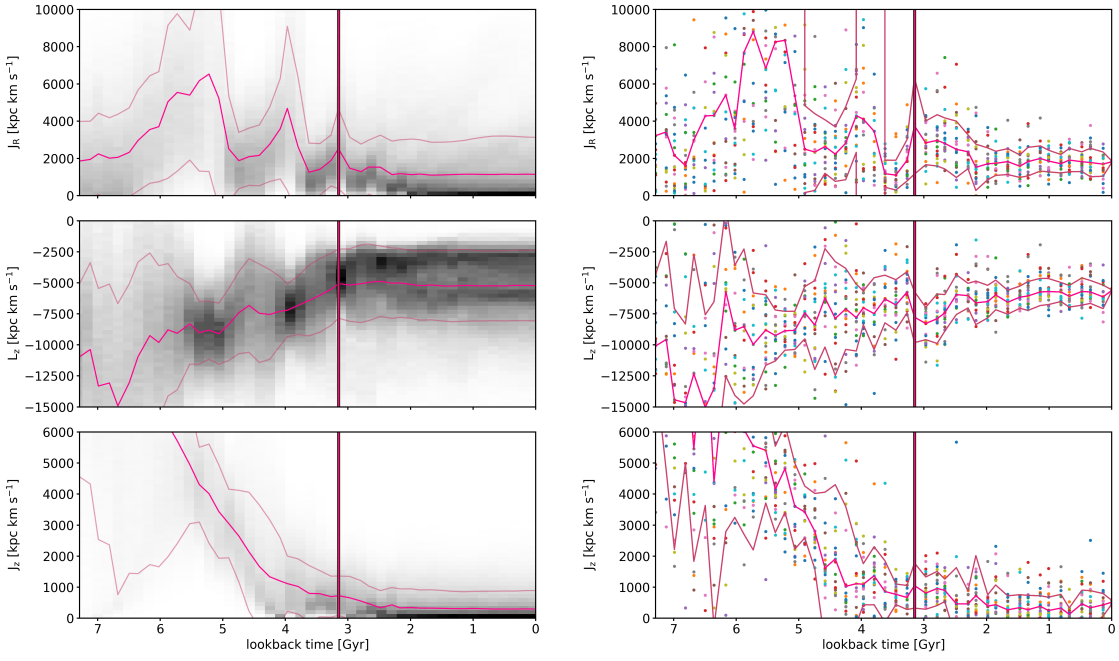


Figure 25: Comparison of overall action evolution (*left panel* - same as Figure 18) with action evolution of particles which are found in a small box in action space (*right panel*). The merger is indicated by the vertical pink line and mean and standard deviations by the other pink lines. The mean in L_z and J_z is similar. The spread is only similar in J_z . In J_R and L_z the spread of the box GCs is smaller. Still, the colored points change a lot and do not stay on constant orbits.

snapshot, we see how close they are in all three actions by construction. But already one snapshot before, they spread out widely and do not have any connection. Going back in time, the spread approximately stays constant. So even though we find similar orbit parameters at the very end, they do not evolve similarly. We compare the evolution of the box particles to the evolution of all accreted particles from prog2. The standard deviations of the actions of the box GCs are slightly lower. The same is done for prog3 and prog4 and gives us similar results.

We constructed a case in which we find a few GCs on similar orbits at the current time as we find them in observations. These could be used to constrain the potential by minimizing their spread. Looking at their time evolution leads to the conclusion that they are only on same orbits right now by chance and will have different properties soon again. So even if constraining the potential by minimizing the spread of accreted GCs in action space would work we need to be careful in the selection of these GCs.

4 Discussion

4.1 Implications

Cold vs hot streams: The assumption that the DF of accreted particles is a δ -function in action space requires them to be on a regular orbit - an assumption that is not fully (e.g. Erkal *et al.*, 2017) but more closely (e.g. Price-Whelan *et al.*, 2016) satisfied for long, cold stellar streams. Already in the introduction we have mentioned, that DG mergers usually create hot stellar streams so our particle streams in Auriga are dynamically hot and have a different, more complex DF. Our results show that trying to constrain the gravitational potential by assuming accreted GCs from one progenitor should cluster in action space does not work. Observers who want to constrain the potential of external galaxies by action-based modelling of tracers need to take this into account and develop this more complex DFs.

Integrals of motion: We find that the integrals of motion, i.e. actions and energy, are not constant during the merger and in their time individual evolution even though the total time evolution stays rather constant. This is also due to more complex perturbations in the accretion process but there could also be dark substructure in the halo which disturbs the orbits.

4.2 Actions of observed dwarf galaxy remnants

It is import to compare results from analysis simulations to observations. One test is looking at our Galaxy, where we have 6D phase space information available, e.g. with *Gaia* (Gaia Collaboration *et al.*, 2016, 2018a), and to see how remnants of a DG merger are distributed in action space.

Recently, Gaia-Enceladus (Helmi *et al.*, 2018), also found by Belokurov *et al.* (2018); Myeong *et al.* (2018) as *Gaia Sausage*, was discovered in the *Gaia* data as an over-density in the Toomre diagram. These are remnant stars of a merger approximately 10 Gyr ago (comparable to prog4) with a mass ratio of 0.24. In contrary to the Sagittarius DG we have precise 6D information from *Gaia* DR2 about Gaia-Enceladus which we need to calculate the actions.

Helmi *et al.* (2018) found Gaia-Enceladus stars in the solar neighbourhood ($d < 2.5 \text{ kpc}$) by selecting them in energy-angular momentum space with $1500 < L_z < 150 \text{ kpc km s}^{-1}$ and $E > 1.8 \cdot 10^5 \text{ km}^2 \text{ s}^{-2}$ assuming a logarithmic halo, a MN disk

and a Hernquist bulge for the MW potential.

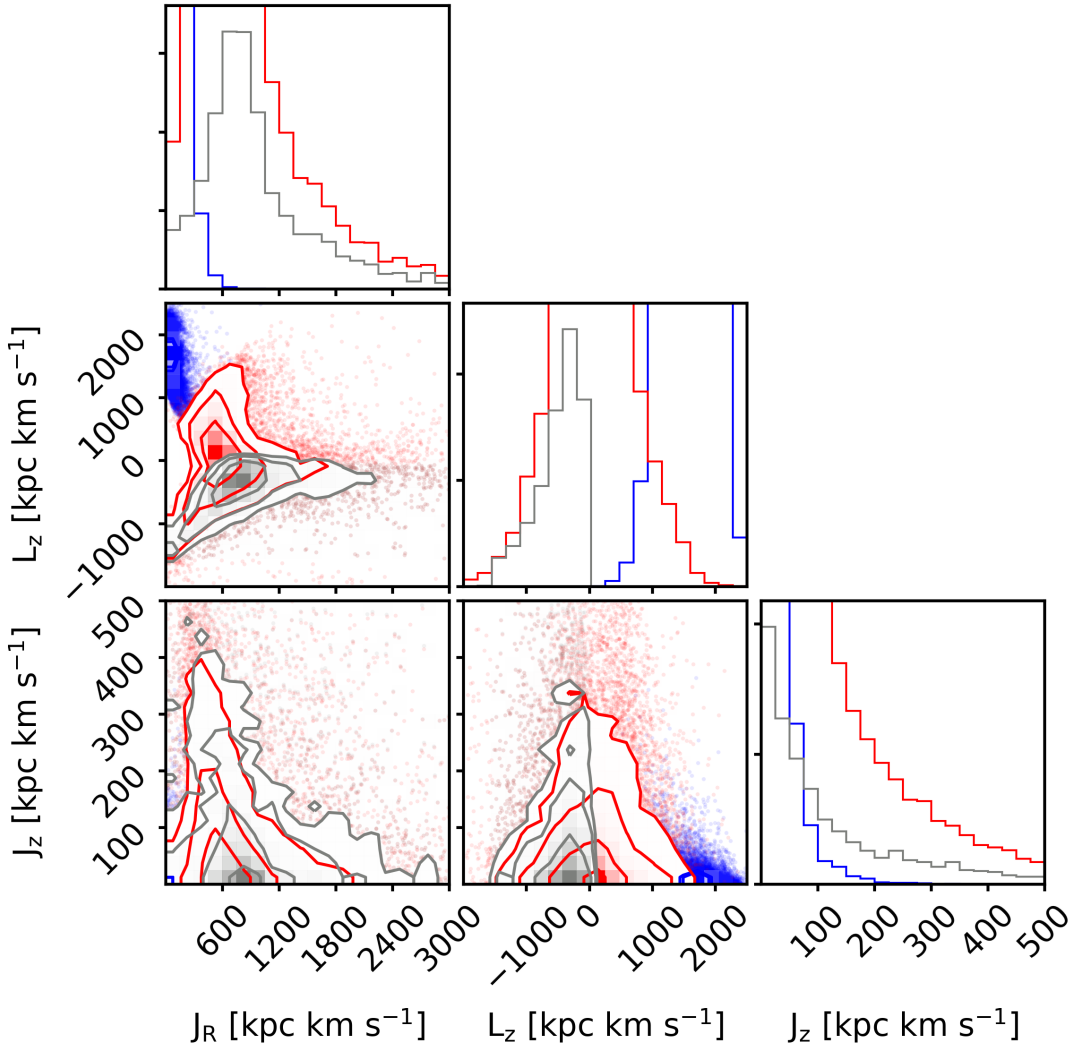


Figure 26: *Gaia*-Enceladus stars in action space in the `MWPotential2014` (Bovy, 2015). The data is taken from *Gaia* DR2 (Gaia Collaboration *et al.*, 2018a) in the MW within $d = 1/\omega < 2.5$ kpc. In blue, actions of disk stars are plotted. The halo including some of the thick disk stars is red. *Gaia*-Enceladus stars are plotted in grey. Disk and halo are clearly distinguishable in angular momentum and also in radial action. *Gaia*-Enceladus is not distinguishable from the halo as it makes up a significant part of it. It has a negative L_z therefore it is counterrotating. It is also very spread out in action space so we cannot detect any sharp features.

In Figure 26, we show actions of the disk, halo and *Gaia*-Enceladus calculated in the `MWPotential2014` (Bovy, 2015). We calculate its actions also in other potentials such as the MW potential from McMillan (2017) and the same potential Helmi *et al.* (2018) applied for their analysis. The distribution does not change. The remnants are neither distinguishable from the halo nor do they make a sharp feature in any of the actions. This tells us that even if there was more dynamical information contained in these stars shortly after the merger, this information vanishes over

time. This confirms our findings that actions of objects accreted from a DG merger cannot be seen as sharp features after some evolution.

4.3 Context in recent research and literature

GCs formation in cosmological simulations

Timo Halbesma (PhD student at the MPA) is working on extracting GCs in the Auriga simulations which have proper physical properties and physically motivated formation recipes. An improvement to this work would e.g. be that he looks for GCs which consist of more than one particle and evolve together as the mass of one stellar particle lies at the very low end of the GC mass regime. Properly selected GCs could clump in action space because their orbits might stay (physically motivated) constant and therefore they could be used to tune the potential right.

The E-MOSAICS simulation suite (Pfeffer *et al.*, 2018; Kruijssen *et al.*, 2018) are zoom-in simulations of the cosmological EAGLE (Schaye *et al.*, 2015) simulations which have implemented models describing the formation, evolution, and disruption of star clusters. In these simulations, Meghan Hughes (PhD student at ESO/LJMU) works on modelling the potential and Sebastian Trujillo-Gomez (Postdoc at ARI) investigates the kinematics of the GCs.

Constraining gravitational potential

There are attempts of applying adaptive dynamics or dynamical modelling with GCs to the MW.

- **DFs of GCs** Posti and Helmi (2019) model the MW's GC system with two DFs, to match the two populations in the disk and the halo. This model constraints the phase-space distribution, the Galactic mass and the shape of the DM halo. Their constraints on the MW mass (see Table 1) lies within the range of the other results. Our method differs in distinguishing GCs from different progenitors and not only into halo or disk. They use more elaborate DFs while our assumption is that the DF is a δ -function.
- **Sharpen stellar streams in simulations to find true potential** Sander-son *et al.* (2015, 2017) investigate stellar streams in cosmological simulations (Aquarius) in action space and try to constrain the gravitational potential by maximizing the amount of clustering. They are successful and can recover the mass profiles. This is very similar to this work. However, they use narrow stellar streams, which are on cold orbits, as tracers while we use GCs accreted from a dynamically hotter progenitor. This could be the reason that their

method gives positive results while ours does not constrain the potential.

- **N-body simulations of accretion of satellites** Jean-Baptiste *et al.* (2017) carried out N-body simulations on merger with satellites including kinematical heating, tidal effects and dynamical friction. In $E - L_z$ space, they found substructure, as expected, but also found multiple satellites to overlap - like prog3 and prog4 in our analysis in action space. Furthermore they found that energy and angular momentum are not conserved during a merger - another conclusion we find in our work in energy and action space. Their work sides with our results.

4.4 Caveats

There are a few assumptions and problems in the course of the investigations which might have influenced the results.

GC selection One of the main problems in the analysis is the GC selection. Aurgia does not resolve GCs and therefore we need to make assumptions and select GC candidates. We applied a very simple recipe which only excluded simulated particles as GC candidates which were in a snapshot in a regime where the stellar disk was very dense and could have destroyed the GC. We carried out the same analysis for different subsets (selected both randomly and specifically through some cuts in the distribution or kinematics). The results were comparable to the ones presented, i.e. the standard deviation in different potentials (Figure 17) and the action evolution for all three progenitors (Figures 18 - 20) showed the same results. However, it would be interesting to see if the properly selected GCs (see Section above) follow the same trends.

Potential fit As we have discussed in Section 2.3, there are a few problems with the potential fit. The bulge-disk decomposition probably underestimates the disk and creates a flaring spatial selection effect. For each component, the model differs from the data especially in the center. This is due to the choice of binning the data, fitting routines, the assumption of spherical or axisymmetry, the simplified potential model consisting of only three analytic building blocks etc. In total, the potential is good enough for the course of our investigations but, as one of the next steps, should be improved.

4.5 Future Work

There are a lot of things which we could not investigate or we had to make compromises on due to the time limitations of this thesis. Big issues which we already discussed are with the potential model and, to a smaller extent, with the GC selection. Improving these recipes would make our analysis more robust. The potential fit could be enhanced by not only fitting spatial properties but also kinematic ones, e.g. the circular velocity. As the vertical profile seems not so well reproduced by the assumed model family, it might be worth experimenting with other disk profiles, superpositions of several MN disks, or non-spherical halo shapes.

`galpy` and `AGAMA` (Vasiliev, 2019) can in principle calculate actions for N -body simulations directly without the need of an analytic gravitational potential. We should compare if the action distribution and evolution behaves as we measured because of their nature and their physical evolution in the simulation (so the calculation of actions in a Stäeckel Fudge or similar approach without the need of an analytic potential first and calculating them in our potential model would give similar results) or because an analytic axisymmetric potential (in general or only our fit) cannot well describe the real potential and messes these things up. Up to now, it was not possible for us to do this step due to technical issues.

The final goal would be to find the right DF of accreted particles which is not yet possible due to numerical (and observational) limitations. If we knew the DF, adaptive dynamics in external galaxies should be a useful method to constrain their gravitational potential. With this true DF and the right gravitational potential, we would know everything about the dynamics of the galaxy.

5 Summary and conclusion

We tested adaptive dynamics in external galaxies to see if it enables us to constrain the potential of these galaxies with the actions of accreted GCs. The idea of adaptive dynamics is to use these accreted particles from the same progenitor to constrain the gravitational potential of the host galaxy. It assumes that the DFs of those objects are δ -functions in action space. Making their action distributions as small as possible should constrain the potential parameters (e.g. mass and shape, depending on the chosen analytic potential).

We did these investigations in a galaxy simulation of the cosmological magnetohydrodynamic Auriga simulation suite. We first fitted an analytic axisymmetric, three component potential model to the simulation motivated by the simplified assumptions dynamical modellers and observers often make to describe external galaxies or the MW. In this potential model, we carried out several test on accreted GCs from DG progenitors in action space. We looked at their action distribution, tried to minimize their spread in action space, investigated the time evolution and picked a small subgroup of GCs which are one similar orbits at the current time to see how they evolved. We carried out several tests, such as energy evolution and analyzing actions in a fixed potential, to make sure our results are not affected by certain assumptions like the GC selection and our potential model. The main conclusions are that,

- fitting an analytic axisymmetric potential to a MW-like simulation is not trivial and requires good techniques but also some compromises. We propose a simple and physically motivated strategy in this work;
- accreted GCs from one progenitor do not move on the same orbit. Their DF is expected to be more complex which would need to be accounted for in dynamical modelling attempts in the future;
- the orbits of these accreted GCs do not stay constant suggesting that various and more complex physical processes are at play in shaping the GC distribution.

Acronyms

AMR	age-metallicity relation
CBE	collisionless Boltzmann equation
CDM	cold dark matter
DF	distribution function
DG	dwarf galaxy
DM	dark matter
DMO	dark matter only
D/T	disk-to-total
GC	globular cluster
IFU	Integral Field Unit
IoMs	integrals of motion
ΛCDM	Lambda cold dark matter
MN	Miyamoto-Nagai
MoND	Modified Newtonian Dynamics
MW	Milky Way
NFW	Navarro-Frenk-White
PM	proper motion
TF	Tully-Fisher

References

- Abadi, M.G., Navarro, J.F., Steinmetz, M., and Eke, V.R. “Simulations of Galaxy Formation in a Λ Cold Dark Matter Universe. II. The Fine Structure of Simulated Galactic Disks”. *ApJ*, **597**, 21–34, 2003.
- Aguilar, L., Hut, P., and Ostriker, J.P. “On the Evolution of Globular Cluster Systems. I. Present Characteristics and Rate of Destruction in Our Galaxy”. *ApJ*, **335**, 720, 1988.
- Bacon, R., Accardo, M., Adjali, L., Anwand, H., Bauer, S., *et al.* “The MUSE second-generation VLT instrument”. In “Ground-based and Airborne Instrumentation for Astronomy III”, volume 7735 of *Society of Photo-Optical Instrumentation Engineers (SPIE) Conference Series*, p. 773508. 2010.
- Baumgardt, H., Hilker, M., Sollima, A., and Bellini, A. “Mean proper motions, space orbits, and velocity dispersion profiles of Galactic globular clusters derived from Gaia DR2 data”. *MNRAS*, **482**, 5138–5155, 2019.
- Belokurov, V., Erkal, D., Evans, N.W., Koposov, S.E., and Deason, A.J. “Co-formation of the disc and the stellar halo”. *MNRAS*, **478**, 611–619, 2018.
- Binney, J. “Modelling the Galaxy for Gaia”. In “The Three-Dimensional Universe with Gaia”, (edited by C. Turon, K.S. O’Flaherty, and M.A.C. Perryman), volume 576 of *ESA Special Publication*, p. 89. 2005.
- Binney, J. “Actions for axisymmetric potentials”. *MNRAS*, **426**, 1324–1327, 2012a.
- Binney, J. “More dynamical models of our Galaxy”. *MNRAS*, **426**, 1328–1337, 2012b.
- Binney, J. and Tremaine, S. *Galactic Dynamics: Second Edition*. 2008.
- Binney, J. and Wong, L.K. “Modelling the Milky Way’s globular cluster system”. *MNRAS*, **467**, 2446–2457, 2017.
- Bland-Hawthorn, J. and Gerhard, O. “The Galaxy in Context: Structural, Kinematic, and Integrated Properties”. *Annual Review of Astronomy and Astrophysics*, **54**, 529–596, 2016.
- Bode, P., Ostriker, J.P., and Turok, N. “Halo Formation in Warm Dark Matter Models”. *ApJ*, **556**, 93–107, 2001.
- Bonaca, A. and Hogg, D.W. “The Information Content in Cold Stellar Streams”. *ApJ*, **867**, 101, 2018.

References

- Bovy, J. “Dynamical Modeling of Tidal Streams”. *ApJ*, **795**, 95, 2014.
- Bovy, J. “galpy: A python Library for Galactic Dynamics”. *The Astrophysical Journal Supplement Series*, **216**, 29, 2015.
- Bovy, J., Bahmanyar, A., Fritz, T.K., and Kallivayalil, N. “The Shape of the Inner Milky Way Halo from Observations of the Pal 5 and GD-1 Stellar Streams”. *ApJ*, **833**, 31, 2016.
- Bovy, J. and Rix, H.W. “A Direct Dynamical Measurement of the Milky Way’s Disk Surface Density Profile, Disk Scale Length, and Dark Matter Profile at 4 kpc $\leq R \leq 9$ kpc”. *ApJ*, **779**, 115, 2013.
- Bowden, A., Belokurov, V., and Evans, N.W. “Dipping our toes in the water: first models of GD-1 as a stream”. *MNRAS*, **449**, 1391–1400, 2015.
- Boylan-Kolchin, M., Bullock, J.S., and Kaplinghat, M. “Too big to fail? The puzzling darkness of massive Milky Way subhaloes”. *MNRAS*, **415**, L40–L44, 2011.
- Bullock, J.S. and Boylan-Kolchin, M. “Small-Scale Challenges to the Λ CDM Paradigm”. *Annual Review of Astronomy and Astrophysics*, **55**, 343–387, 2017.
- Callingham, T., Cautun, M., Deason, A.J., Frenk, C.S., Wang, W., Gómez, F.A., Grand, R.J.J., Marinacci, F., and Pakmor, R. “The mass of the Milky Way from satellite dynamics”. *ArXiv e-prints*, arXiv:1808.10456, 2018.
- Cappellari, M. “Measuring the inclination and mass-to-light ratio of axisymmetric galaxies via anisotropic Jeans models of stellar kinematics”. *MNRAS*, **390**, 71–86, 2008.
- Carroll, B.W. and Ostlie, D.A. *An introduction to modern astrophysics and cosmology*. 2006.
- Clowe, D., Bradač, M., Gonzalez, A.H., Markevitch, M., Randall, S.W., Jones, C., and Zaritsky, D. “A Direct Empirical Proof of the Existence of Dark Matter”. *ApJ*, **648**, L109–L113, 2006.
- Davis, M., Efstathiou, G., Frenk, C.S., and White, S.D.M. “The evolution of large-scale structure in a universe dominated by cold dark matter”. *ApJ*, **292**, 371–394, 1985.
- de Zeeuw, T. “Elliptical galaxies with separable potentials”. *MNRAS*, **216**, 273–334, 1985.

- Dierickx, M.I.P. and Loeb, A. “An Upper Limit on the Milky Way Mass from the Orbit of the Sagittarius Dwarf Satellite”. *ApJ*, **847**, 42, 2017.
- Dubinski, J. and Carlberg, R.G. “The Structure of Cold Dark Matter Halos”. *ApJ*, **378**, 496, 1991.
- Eadie, G. and Jurić, M. “The cumulative mass profile of the Milky Way as determined by globular cluster kinematics from Gaia DR2”. *arXiv e-prints*, arXiv:1810.10036, 2018.
- Eilers, A.C., Hogg, D.W., Rix, H.W., and Ness, M. “The Circular Velocity Curve of the Milky Way from \$5\\$ to \\$25\\$ kpc”. *arXiv e-prints*, arXiv:1810.09466, 2018.
- Emsellem, E., Monnet, G., and Bacon, R. “The multi-gaussian expansion method: a tool for building realistic photometric and kinematical models of stellar systems I. The formalism”. *A&A*, **285**, 723–738, 1994.
- Erkal, D., Koposov, S.E., and Belokurov, V. “A sharper view of Pal 5’s tails: discovery of stream perturbations with a novel non-parametric technique”. *MNRAS*, **470**, 60–84, 2017.
- Eyre, A. and Binney, J. “The mechanics of tidal streams”. *MNRAS*, **413**, 1852–1874, 2011.
- Faber, S.M. and Jackson, R.E. “Velocity dispersions and mass-to-light ratios for elliptical galaxies.” *ApJ*, **204**, 668–683, 1976.
- Ferrero, I., Abadi, M.G., Navarro, J.F., Sales, L.V., and Gurovich, S. “The dark matter haloes of dwarf galaxies: a challenge for the Λ cold dark matter paradigm?” *MNRAS*, **425**, 2817–2823, 2012.
- Flores, R.A. and Primack, J.R. “Observational and Theoretical Constraints on Singular Dark Matter Halos”. *ApJ*, **427**, L1, 1994.
- Foreman-Mackey, D., Hogg, D.W., Lang, D., and Goodman, J. “emcee: The MCMC Hammer”. *Publications of the Astronomical Society of the Pacific*, **125**, 306, 2013.
- Gaia Collaboration, Brown, A.G.A., Vallenari, A., Prusti, T., de Bruijne, J.H.J., *et al.* “Gaia Data Release 2. Summary of the contents and survey properties”. *A&A*, **616**, A1, 2018a.
- Gaia Collaboration, Helmi, A., van Leeuwen, F., McMillan, P.J., Massari, D., *et al.* “Gaia Data Release 2. Kinematics of globular clusters and dwarf galaxies around the Milky Way”. *A&A*, **616**, A12, 2018b.

References

- Gaia Collaboration, Prusti, T., de Bruijne, J.H.J., Brown, A.G.A., Vallenari, A., *et al.* “The Gaia mission”. *A&A*, **595**, A1, 2016.
- Geehan, J.J., Fardal, M.A., Babul, A., and Guhathakurta, P. “Investigating the Andromeda stream - I. Simple analytic bulge-disc-halo model for M31”. *MNRAS*, **366**, 996–1011, 2006.
- Gibbons, S.L.J., Belokurov, V., and Evans, N.W. “‘Skinny Milky Way please’, says Sagittarius”. *MNRAS*, **445**, 3788–3802, 2014.
- Grand, R.J.J., Gómez, F.A., Marinacci, F., Pakmor, R., Springel, V., Campbell, D.J.R., Frenk, C.S., Jenkins, A., and White, S.D.M. “The Auriga Project: the properties and formation mechanisms of disc galaxies across cosmic time”. *MNRAS*, **467**, 179–207, 2017.
- Helmi, A., Babusiaux, C., Koppelman, H.H., Massari, D., Veljanoski, J., and Brown, A.G.A. “The merger that led to the formation of the Milky Way’s inner stellar halo and thick disk”. *Nature*, **563**, 85–88, 2018.
- Helmi, A. and White, S.D.M. “Building up the stellar halo of the Galaxy”. *MNRAS*, **307**, 495–517, 1999.
- Hernquist, L. “An Analytical Model for Spherical Galaxies and Bulges”. *ApJ*, **356**, 359, 1990.
- Ibata, R.A., Gilmore, G., and Irwin, M.J. “A dwarf satellite galaxy in Sagittarius”. *Nature*, **370**, 194–196, 1994.
- Jean-Baptiste, I., Di Matteo, P., Haywood, M., Gómez, A., Montuori, M., Combes, F., and Semelin, B. “On the kinematic detection of accreted streams in the Gaia era: a cautionary tale”. *A&A*, **604**, A106, 2017.
- Jeans, J.H. “On the theory of star-streaming and the structure of the universe”. *MNRAS*, **76**, 70–84, 1915.
- Johnston, K.V., Zhao, H., Spergel, D.N., and Hernquist, L. “Tidal Streams as Probes of the Galactic Potential”. *ApJ*, **512**, L109–L112, 1999.
- Jones, E., Oliphant, T., Peterson, P., *et al.* “SciPy: Open source scientific tools for Python”. 2001. [Online; accessed <today>].
- Kaiser, N. and Squires, G. “Mapping the Dark Matter with Weak Gravitational Lensing”. *ApJ*, **404**, 441, 1993.

- Kirby, E.N., Bullock, J.S., Boylan-Kolchin, M., Kaplinghat, M., and Cohen, J.G. “The dynamics of isolated Local Group galaxies”. *MNRAS*, **439**, 1015–1027, 2014.
- Klypin, A., Kravtsov, A.V., Valenzuela, O., and Prada, F. “Where Are the Missing Galactic Satellites?” *ApJ*, **522**, 82–92, 1999.
- Koposov, S.E., Rix, H.W., and Hogg, D.W. “Constraining the Milky Way Potential with a Six-Dimensional Phase-Space Map of the GD-1 Stellar Stream”. *ApJ*, **712**, 260–273, 2010.
- Kruijssen, J.M.D., Pfeffer, J.L., Reina-Campos, M., Crain, R.A., and Bastian, N. “The formation and assembly history of the Milky Way revealed by its globular cluster population”. *MNRAS*, p. 1537, 2018.
- Küpper, A.H.W., Balbinot, E., Bonaca, A., Johnston, K.V., Hogg, D.W., Kroupa, P., and Santiago, B.X. “Globular Cluster Streams as Galactic High-Precision Scales—the Poster Child Palomar 5”. *ApJ*, **803**, 80, 2015.
- Küpper, A.H.W., Kroupa, P., Baumgardt, H., and Heggie, D.C. “Tidal tails of star clusters”. *MNRAS*, **401**, 105–120, 2010.
- Küpper, A.H.W., Lane, R.R., and Heggie, D.C. “More on the structure of tidal tails”. *MNRAS*, **420**, 2700–2714, 2012.
- Law, D.R. and Majewski, S.R. “The Sagittarius Dwarf Galaxy: A Model for Evolution in a Triaxial Milky Way Halo”. *ApJ*, **714**, 229–254, 2010.
- Leaman, R., Vandenberg, D.A., and Mendel, J.T. “The bifurcated age-metallicity relation of Milky Way globular clusters and its implications for the accretion history of the galaxy”. *MNRAS*, **436**, 122–135, 2013.
- Malhan, K. and Ibata, R.A. “Constraining the Milky Way Halo Potential with the GD-1 stellar stream”. *arXiv e-prints*, arXiv:1807.05994, 2018.
- Maoz, D. *Astrophysics in a Nutshell*. 2007.
- McMillan, P.J. “The mass distribution and gravitational potential of the Milky Way”. *MNRAS*, **465**, 76–94, 2017.
- Milgrom, M. “A modification of the Newtonian dynamics as a possible alternative to the hidden mass hypothesis.” *ApJ*, **270**, 365–370, 1983.
- Misgeld, I. and Hilker, M. “Families of dynamically hot stellar systems over 10 orders of magnitude in mass”. *MNRAS*, **414**, 3699–3710, 2011.

References

- Miyamoto, M. and Nagai, R. “Three-dimensional models for the distribution of mass in galaxies.” *Publications of the Astronomical Society of Japan*, **27**, 533–543, 1975.
- Mo, H., van den Bosch, F.C., and White, S. *Galaxy Formation and Evolution*. 2010.
- Monnet, G., Bacon, R., and Emsellem, E. “Modelling the stellar intensity and radial velocity fields in triaxial galaxies by sums of Gaussian functions.” *A&A*, **253**, 366–373, 1992.
- Moore, B. “Evidence against dissipation-less dark matter from observations of galaxy haloes”. *Nature*, **370**, 629–631, 1994.
- Moore, B., Ghigna, S., Governato, F., Lake, G., Quinn, T., Stadel, J., and Tozzi, P. “Dark Matter Substructure within Galactic Halos”. *ApJ*, **524**, L19–L22, 1999.
- Moreno, E., Pichardo, B., and Velázquez, H. “Tidal Radii and Destruction Rates of Globular Clusters in the Milky Way due to Bulge-Bar and Disk Shocking”. *ApJ*, **793**, 110, 2014.
- Myeong, G.C., Evans, N.W., Belokurov, V., Sanders, J.L., and Koposov, S.E. “The Sausage Globular Clusters”. *ApJ*, **863**, L28, 2018.
- Navarro, J.F., Frenk, C.S., and White, S.D.M. “The Structure of Cold Dark Matter Halos”. *ApJ*, **462**, 563, 1996.
- Navarro, J.F., Frenk, C.S., and White, S.D.M. “A Universal Density Profile from Hierarchical Clustering”. *ApJ*, **490**, 493–508, 1997.
- Newberg, H.J., Willett, B.A., Yanny, B., and Xu, Y. “The Orbit of the Orphan Stream”. *ApJ*, **711**, 32–49, 2010.
- Ostriker, J.P. and Steinhardt, P. “New Light on Dark Matter”. *Science*, **300**, 1909–1914, 2003.
- Papastergis, E., Giovanelli, R., Haynes, M.P., and Shankar, F. “Is there a ”too big to fail” problem in the field?” *A&A*, **574**, A113, 2015.
- Papastergis, E. and Shankar, F. “An assessment of the ”too big to fail” problem for field dwarf galaxies in view of baryonic feedback effects”. *A&A*, **591**, A58, 2016.
- Pfeffer, J., Kruijssen, J.M.D., Crain, R.A., and Bastian, N. “The E-MOSAICS project: simulating the formation and co-evolution of galaxies and their star cluster populations”. *MNRAS*, **475**, 4309–4346, 2018.
- Planck Collaboration, Aghanim, N., Akrami, Y., Ashdown, M., Aumont, J.,

- et al.* “Planck 2018 results. VI. Cosmological parameters”. *arXiv e-prints*, arXiv:1807.06209, 2018.
- Pontzen, A. and Governato, F. “How supernova feedback turns dark matter cusps into cores”. *MNRAS*, **421**, 3464–3471, 2012.
- Posti, L. and Helmi, A. “Mass and shape of the Milky Way’s dark matter halo with globular clusters from Gaia and Hubble”. *A&A*, **621**, A56, 2019.
- Price-Whelan, A.M., Johnston, K.V., Valluri, M., Pearson, S., Küpper, A.H.W., and Hogg, D.W. “Chaotic dispersal of tidal debris”. *MNRAS*, **455**, 1079–1098, 2016.
- Renaud, F., Agertz, O., and Gieles, M. “The origin of the Milky Way globular clusters”. *MNRAS*, **465**, 3622–3636, 2017.
- Rix, H.W., de Zeeuw, P.T., Cretton, N., van der Marel, R.P., and Carollo, C.M. “Dynamical Modeling of Velocity Profiles: The Dark Halo around the Elliptical Galaxy NGC 2434”. *ApJ*, **488**, 702–719, 1997.
- Rubin, V.C., Ford, W. K., J., and Thonnard, N. “Extended rotation curves of high-luminosity spiral galaxies. IV. Systematic dynamical properties, Sa -> Sc.” *ApJ*, **225**, L107–L111, 1978.
- Rubin, V.C., Ford, W. K., J., and Thonnard, N. “Rotational properties of 21 SC galaxies with a large range of luminosities and radii, from NGC 4605 ($R=4\text{kpc}$) to UGC 2885 ($R=122\text{kpc}$).” *ApJ*, **238**, 471–487, 1980.
- Rubin, V.C. and Ford, W. Kent, J. “Rotation of the Andromeda Nebula from a Spectroscopic Survey of Emission Regions”. *ApJ*, **159**, 379, 1970.
- Sanders, J. “Angle-action estimation in a general axisymmetric potential”. *MNRAS*, **426**, 128–139, 2012.
- Sanders, J.L. “Probabilistic model for constraining the Galactic potential using tidal streams”. *MNRAS*, **443**, 423–431, 2014.
- Sanders, J.L. and Binney, J. “A review of action estimation methods for galactic dynamics”. *MNRAS*, **457**, 2107–2121, 2016.
- Sanderson, R.E., Hartke, J., and Helmi, A. “Modeling the Gravitational Potential of a Cosmological Dark Matter Halo with Stellar Streams”. *ApJ*, **836**, 234, 2017.
- Sanderson, R.E., Helmi, A., and Hogg, D.W. “Action-space Clustering of Tidal Streams to Infer the Galactic Potential”. *ApJ*, **801**, 98, 2015.

References

- Sarzi, M., Iodice, E., Coccato, L., Corsini, E.M., de Zeeuw, P.T., *et al.* “Fornax3D project: Overall goals, galaxy sample, MUSE data analysis, and initial results”. *A&A*, **616**, A121, 2018.
- Sawala, T., Frenk, C.S., Fattahi, A., Navarro, J.F., Bower, R.G., *et al.* “The APOSTLE simulations: solutions to the Local Group’s cosmic puzzles”. *MNRAS*, **457**, 1931–1943, 2016.
- Schaye, J., Crain, R.A., Bower, R.G., Furlong, M., Schaller, M., *et al.* “The EAGLE project: simulating the evolution and assembly of galaxies and their environments”. *MNRAS*, **446**, 521–554, 2015.
- Schneider, A., Smith, R.E., and Reed, D. “Halo mass function and the free streaming scale”. *MNRAS*, **433**, 1573–1587, 2013.
- Schwarzschild, M. “A numerical model for a triaxial stellar system in dynamical equilibrium.” *ApJ*, **232**, 236–247, 1979.
- Smith, R.E. and Markovic, K. “Testing the warm dark matter paradigm with large-scale structures”. *Phys. Rev. D*, **84**, 063507, 2011.
- Sohn, S.T., Watkins, L.L., Fardal, M.A., van der Marel, R.P., Deason, A.J., Besla, G., and Bellini, A. “Absolute Hubble Space Telescope Proper Motion (HST-PROMO) of Distant Milky Way Globular Clusters: Galactocentric Space Velocities and the Milky Way Mass”. *ApJ*, **862**, 52, 2018.
- Springel, V. “E pur si muove: Galilean-invariant cosmological hydrodynamical simulations on a moving mesh”. *MNRAS*, **401**, 791–851, 2010.
- Springel, V., White, S.D.M., Jenkins, A., Frenk, C.S., Yoshida, N., *et al.* “Simulations of the formation, evolution and clustering of galaxies and quasars”. *Nature*, **435**, 629–636, 2005.
- Tollerud, E.J., Boylan-Kolchin, M., and Bullock, J.S. “M31 satellite masses compared to Λ CDM subhaloes”. *MNRAS*, **440**, 3511–3519, 2014.
- Tremaine, S. “The geometry of phase mixing”. *MNRAS*, **307**, 877–883, 1999.
- Trick, W. *Action-based Dynamical Modeling for the Milky Way Disk*. Ph.D. thesis, University of Heidelberg, 2017.
- Trick, W.H., Bovy, J., and Rix, H.W. “Action-Based Dynamical Modeling for the Milky Way Disk”. *ApJ*, **830**, 97, 2016a.

- Trick, W.H., van de Ven, G., and Dutton, A.A. “A spiral galaxy’s mass distribution uncovered through lensing and dynamics”. MNRAS, **463**, 3151–3168, 2016b.
- Tully, R.B. and Fisher, J.R. “Reprint of 1977A&A....54..661T. A new method of determining distance to galaxies.” A&A, **500**, 105–117, 1977.
- Tyson, J.A., Valdes, F., and Wenk, R.A. “Detection of Systematic Gravitational Lens Galaxy Image Alignments: Mapping Dark Matter in Galaxy Clusters”. ApJ, **349**, L1, 1990.
- van de Ven, G., Falcón-Barroso, J., McDermid, R.M., Cappellari, M., Miller, B.W., and de Zeeuw, P.T. “The Einstein Cross: Constraint on Dark Matter from Stellar Dynamics and Gravitational Lensing”. ApJ, **719**, 1481–1496, 2010.
- van den Bosch, R.C.E., van de Ven, G., Verolme, E.K., Cappellari, M., and de Zeeuw, P.T. “Triaxial orbit based galaxy models with an application to the (apparent) decoupled core galaxy NGC 4365”. MNRAS, **385**, 647–666, 2008.
- Vanhollebeke, E., Groenewegen, M.A.T., and Girardi, L. “Stellar populations in the Galactic bulge. Modelling the Galactic bulge with TRILEGAL”. A&A, **498**, 95–107, 2009.
- Vasiliev, E. “A new code for orbit analysis and Schwarzschild modelling of triaxial stellar systems”. MNRAS, **434**, 3174–3195, 2013.
- Vasiliev, E. “Proper motions and dynamics of the Milky Way globular cluster system from Gaia DR2”. *arXiv e-prints*, arXiv:1807.09775, 2018.
- Vasiliev, E. “AGAMA: action-based galaxy modelling architecture”. MNRAS, **482**, 1525–1544, 2019.
- Watkins, L.L., van der Marel, R.P., Sohn, S.T., and Evans, N.W. “Evidence for an Intermediate-Mass Milky Way from Gaia DR2 Halo Globular Cluster Motions”. *ArXiv e-prints*, arXiv:1804.11348, 2018.
- Zhu, L., Ven, G.v.d., Bosch, R.v.d., Rix, H.W., Lyubenova, M., *et al.* “The stellar orbit distribution in present-day galaxies inferred from the CALIFA survey”. *Nature Astronomy*, **2**, 233–238, 2018.
- Zwicky, F. “Die Rotverschiebung von extragalaktischen Nebeln”. *Helvetica Physica Acta*, **6**, 110–127, 1933.

Thank you,

Glenn van de Ven, for giving me the opportunity to join you at ESO, to work again in the exciting field of dynamics, for your scientific insight, for supporting me in my work and in my scientific development and for generally believing in me.

Ralf Klessen, for evaluating my thesis.

Wilma Trick, for your inspiring ideas for this project, for giving me scientific freedom and being patient with me, for your support in the ups and downs of this project, for providing me with many helpful advices and for believing in me when I did not. Thank you for your great supervision!

Timo Halbesma, for helping me with the technical set-up, issues and difficulties.

Laura Watkins and Prashin Jethwa, for proofreading my thesis and for very helpful advice on my science and career.

Volker Springel, for providing me with the excellent Auriga simulations.

Jo Bovy, for providing galpy which I heavily used for my investigations.

the European Southern Observatory and the “Galaxy Dynamics” research group in Heidelberg and Garching, for providing such a friendly and scientifically inspiring environment and many helpful colleagues.

the European Research Council, for funding from the European Research Council (ERC) under the European Union’s Horizon 2020 research and innovation programme under grant agreement No 724857 (Consolidator Grant ArcheoDyn).

"ESO 5th floor", for making my time at ESO fun and happy.

my parents Sigrun and Ivo, for supporting me in everything.

my brother and best friend Niko, for always being there.

Statement

This thesis is my own work and I have only used the sources indicated. Where the work of others has been quoted or reproduced, the source is always given.

Heidelberg, January 18, 2019